January 2012

Design of a Pneumatic Stepper Motor for MRI Environments

Grant Cameron McDonald
Worcester Polytechnic Institute

Gregory J. Overton
Worcester Polytechnic Institute

Kellen C. Pastore
Worcester Polytechnic Institute

Analysis and Performance of a Pneumatic Stepper Motor for Use in MRI Environments

A Robotics Engineering MQP

Grant McDonald

Greg Overton

Kellen Pastore

Advised by

Prof. Gregory Fischer

Gregory Cole

12/5/2011

Modern medicine promotes the design and creation of innovative ideas. The goal of this project is to further the research in MRI compatible actuators. The proposed actuator design, known as the Pneumatically Ratcheting Stepper Motor (PRiSM), uses directed pneumatic pressure to generate rotational motion. To confirm the validity of this idea, multiple tests were designed and conducted. These tests show that, at 60psi, the PRiSM can operate open-loop with an angular velocity of 7deg/s, while exerting a torque of 435N/mm. Optimized conditions yielded an overall maximum angular velocity of 178deg/s and an overall maximum torque of 747N/mm.

Table of Contents

Table of Figures

List of Tables

Introduction

Image Guided Intervention (IGI) has been identified as having the potential to impact the effectiveness of many medical procedures, including: biopsies, liver ablation, and tumor treatment (Staff, 2008). Great strides have been made toward creating MRI-compatible actuators for this purpose. The PneuStep, developed at John Hopkins University, is an example of this form of actuation (Johns Hopkins Medicine, 2005). The PneuStep has been shown to operate in an MRI environment, without causing image distortion.

In this project a similar pneumatic motor was designed to both be functional in an MRI machine, and to improve upon performance metrics of existing pneumatic motors. The goal was to produce a reliable, scalable, high-precision motor out of MRI-compatible (non-ferrous, dielectric) materials. Ferrous materials are dangerous to have in MRI machines, and can cause injuries to persons inside the machine. (Mallot, 1997) The design presented in this report, the Pneumatically Ratcheting Stepper Motor (PRiSM), achieves this goal. The PRiSM design works by concentrating pneumatic pressure, in a cyclic manner, on a number of drive pistons. These pistons, in turn, articulate a drive gear which serves as the motor output. To evaluate the performance of the PRiSM, numerous tests were designed which benchmarked the PRiSM against theoretical and existing performance metrics.

The PRiSM was evaluated for two main characteristics, the maximum open-loop and maximum possible speeds, and the maximum torque output. The speed testing discussed in this report is based on open-loop reliability. This was to ensure the open-loop potential of the motor while the torque was tested for the maximum output.

After testing the motor it was determined that the PRiSM effectively demonstrates a new motor design, which is fully MRI compatible. The PRiSM is also largely scalable and versatile, its design allowing for optimization based upon the application.

Background Research

Magnetic Resonance Imaging (MRI) compatible robotic devices and systems have started to become a more popular topic of modern medicine. The goal is to utilize MRI imaging to increase the reliability and effectiveness of precision surgery. This field is known as Image Guided Intervention (IGI). MRI machines are used to visualize internal anatomical structures with precision. Along with this precision the MRI can show variation in density in these internal structures which allows for the differentiation between various body tissues and bones. Modern medicine has been working toward using MRI technology not only to diagnose, but also to treat illnesses through guided surgical intervention. When designing any instrument intended for use in an MRI environment, one must consider the high magnetic field strength inherent in the machine. Along with the limited nature of permissible materials, the MRI bore has very limited cross-sectional area, creating a constraint on device sizing (Gassert, Burdet, & Chinzei, 2008). Two types of actuation are currently being used in MRI instruments: piezoelectric and pneumatic systems (Fischer, Krieger, Iordachita, Csorra, Whitcomb, & Fichtinger, 2008).

Piezoelectric motors operate by electrically inducing vibration in a ceramic material, which in turn is used to create either linear or rotational motion. An example of an approach to creating linear motion is the piezostack, Figure 1 (Tse, Chan, Janssen, Hamed, Young, & Lamperth).

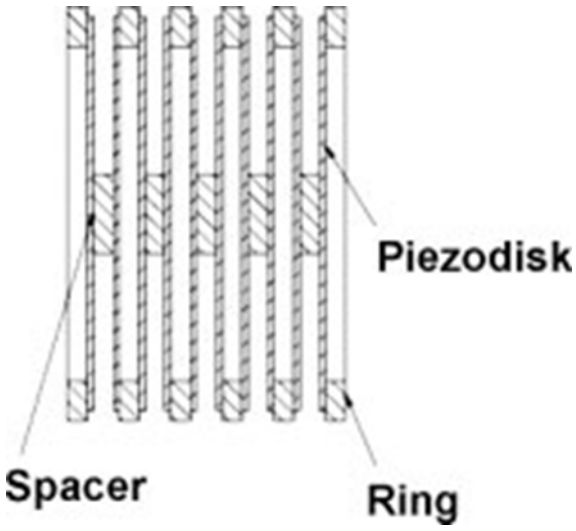

Figure 1: Piezostack

A piezostack is composed of multiple piezodisks layered on top of one another. When power is supplied to the piezostack the individual piezodisks elongate, creating linear motion (Tse, Chan, Janssen, Hamed, Young, & Lamperth). One application of linear motion is MR elastography, a medical procedure

used to diagnose tumors. A piezoelectric actuator designed in this manner (shown in Figure 2) provided a minimal artifact of 7.9mm, with a signal-to-noise ratio loss of 7.9% (Tse, Chan, Janssen, Hamed, Young, & Lamperth). This device was controlled and operated through the use of a National Instruments cRIO. The cRIO provided one way of producing the frequency used to control the piezostack (Tse, Chan, Janssen, Hamed, Young, & Lamperth).

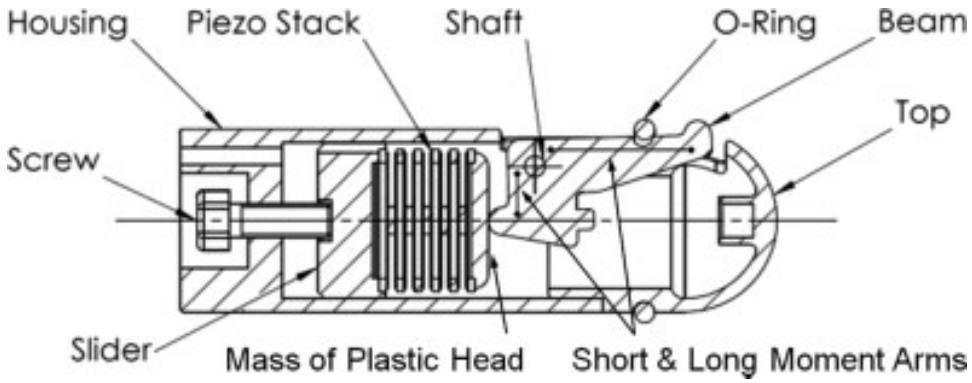

Figure 2: MR Elastography Device

The cost of piezoelectric motor drivers is prohibitively expensive and allows for limited driving frequencies (Wang, Cole, Su, Pilitis, & Fischer, 2009). One method for producing the necessary driving frequencies is the implementation of custom piezoelectric drivers, such as what was done for the Piezoelectric Actuator System for the Neural Intervention Robot shown in Figure 3 (Wang, Cole, Su, Pilitis, & Fischer, 2009).

Figure 3: Neural Intervention Robot

Custom driver implementation is a process that takes significant development time and funding. Despite the cost and time required, these drivers allow for a very low signal-to-noise ratio loss (less than 3% in a 3T scanner) (Wang, Cole, Su, Pilitis, & Fischer, 2009). Shielding components and a carefully designed control system allows the Neural Intervention Robot's piezoelectric actuators to operate with minimal MRI interference (Wang, Cole, Su, Pilitis, & Fischer, 2009). The same type of piezoelectric driver was used with the MRI-Guided Needle Placement Robot (Su, Zervas, Cole, Furlong, & Fischer, 2011). In both cases, the drivers operated the piezoelectric actuators in the MRI environment with minimal interference (Wang, Cole, Su, Pilitis, & Fischer, 2009) (Su, Zervas, Cole, Furlong, & Fischer, 2011).

Another form of MRI compatible actuation is a pneumatic system. Pneumatic actuators operate using controlled air flow to produce motion. An MRI compatible Pneumatic Robot for Transperineal Prostate Needle Placement uses pneumatic power to accurately place a needle, Figure 4 (Fischer, et al., 2008). One issue this project had was the absence of MRI compatible pneumatic cylinders (Fischer, et al., 2008). To overcome this problem the team developed a custom pneumatic cylinder. The cylinder was constructed out of glass and used a graphite piston. One issue with these materials is that they lack stability; to counteract this problem a pneumatic brake was implemented to increase the rigidity of the system. The accuracy and repeatability of this device was critical in the performance ratings of the

medical industry (Gassert, Burdet, & Chinzei, 2008). While the Pneumatic Robot for Transperineal Prostate Needle Placement addresses a current challenge in medicine, other innovative concepts and designs in pneumatic actuation are continually being developed.

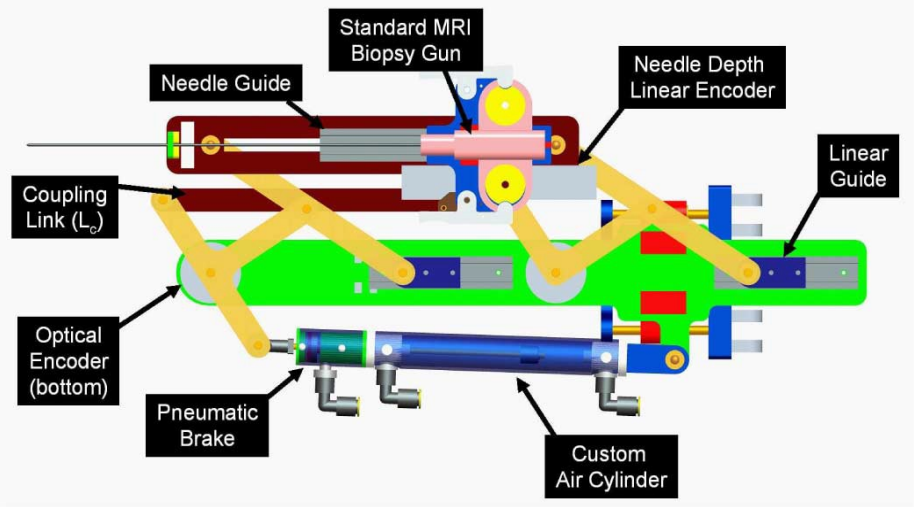

Figure 4: MRI compatible Pneumatic Robot for Transperineal Prostate Needle Placement

One of these designs is the MRI Compatible Rigid and Flexible Outer Sheath device (Zuo, et al., 2008). The device focuses on providing a method of performing minimally invasive endoscopic surgery with the use of MRI guidance. The device has two operating modes:, flexible and rigid. When the device is in flexible operating mode, the system's vacuum unit keeps the internal and external pressures equal. With these pressures equal, the toothed links disengage from the bellows tube and allow the device to move freely, Figure 5.

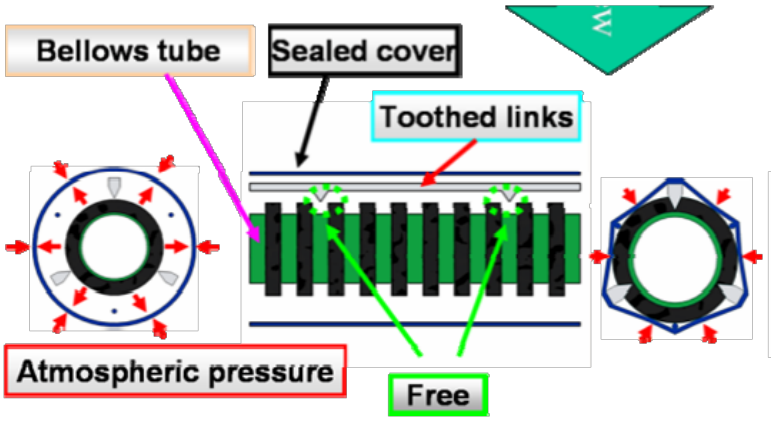

Figure 5: Flexible Mode

The rigid operating mode occurs when the vacuum removes air from the system, pressing the toothed links into the bellows tube. This operation locks the rigid outer sheath device into place as shown in Figure 6.

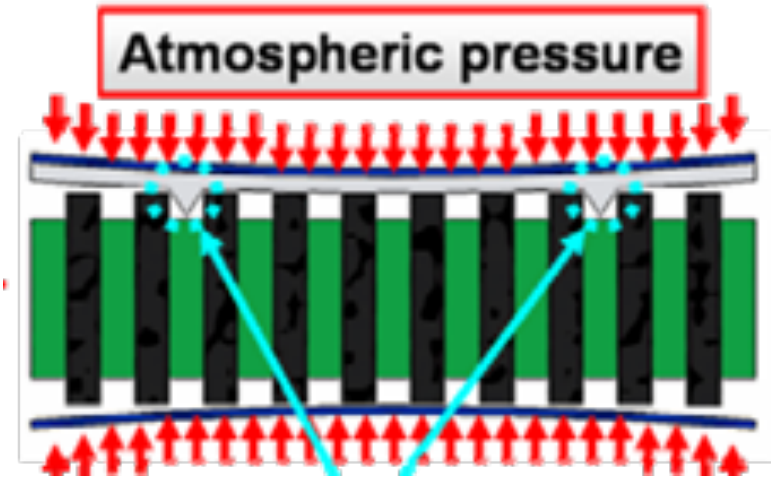

Figure 6: Rigid Mode

The 300mm long device can contort into the shape of an "S" using its vacuum system in rigid operation, Figure 7 (Zuo, et al., 2008). When introduced within an MRI environment the Outer Sheath device showed a signal-to-noise ratio loss of 4.3%.

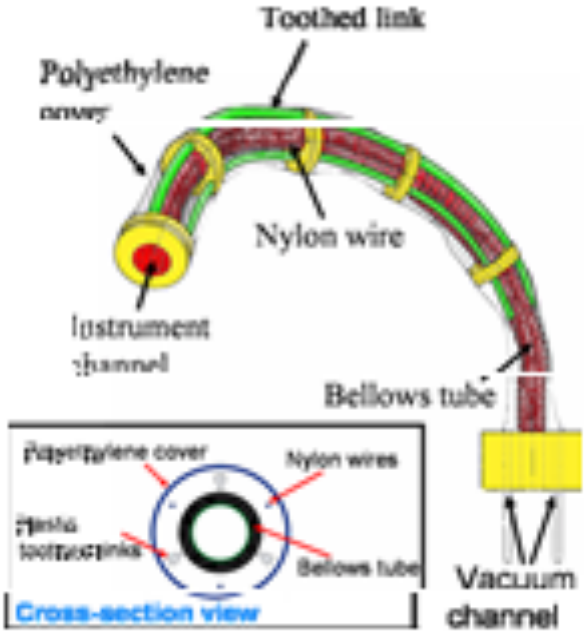

Figure 7: In Operation

Lastly, it is important to discuss the closest analog to the PRiSM, the PneuStep. Developed at Johns Hopkins University, and published in 2007 (Johns Hopkins Medicine, 2005). The PneuStep

demonstrates that precise and discrete positions can be achieved using pneumatic systems. Additionally, it demonstrates that this precision can be implemented in high-intensity MRI environments. Figure 8 shows a diagram of their design, taken from a conference paper published in the IEEE/ASME Mechatronics conference in 2007.

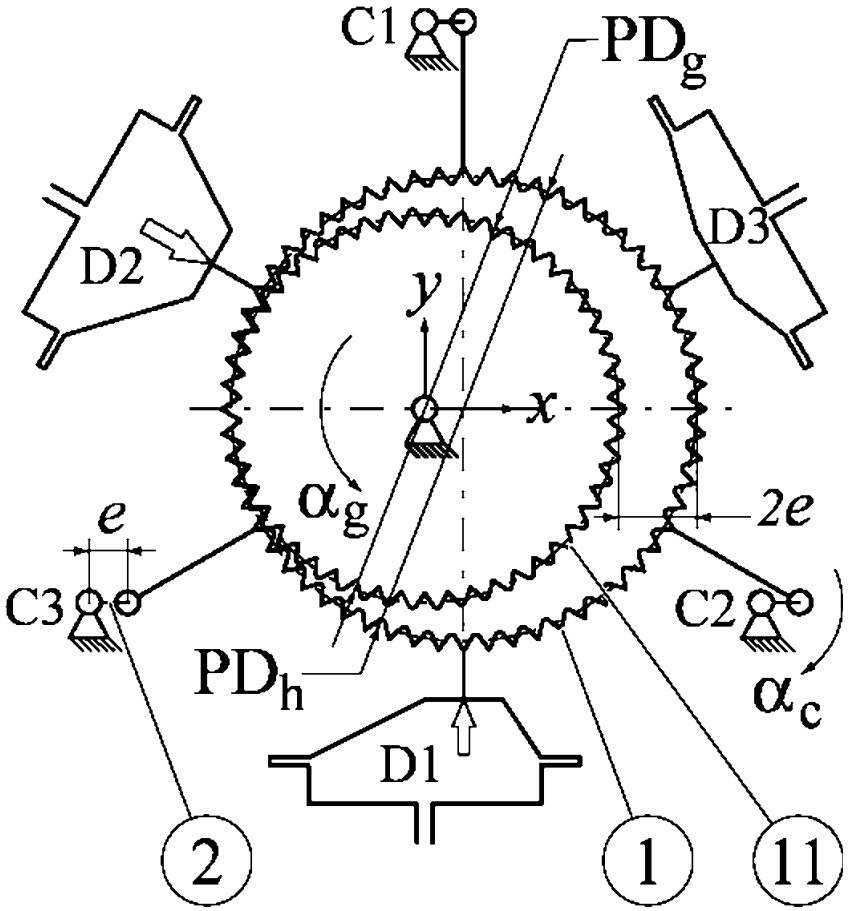

Figure 8: PneuStep Model

Motion is induced by inflating diaphragms D1, D2, and D3 sequentially. These diaphragms impart force on an internal-tooth ring gear, PD_h, which translates in a circular path due to the triple-parallel mechanism composed of cranks C1, C2, and C3. The drive gear, PD_g, is fixed on a central rotational axis at *x, y*. As the ring gear translates, it remains fully engaged with the drive gear, which then serves as a mechanical transformer and as the output from the motor. A picture of two assembled PneuSteps can be seen in Figure 9.

Figure 9: Two different sizes of the PneuStep

The PneuStep was used as the actuator in the first fully MRI-compatible robot, designed to allow for MRI guidance of transperineal percutaneous needle placement. The robot showed no interference with the MRI imager while stationary or while moving in both standard 3T MRI imagers and in a stronger 7T MRI imager. Figure 10 shows this robot assembled and mounted on the bed of an MRI scanner.

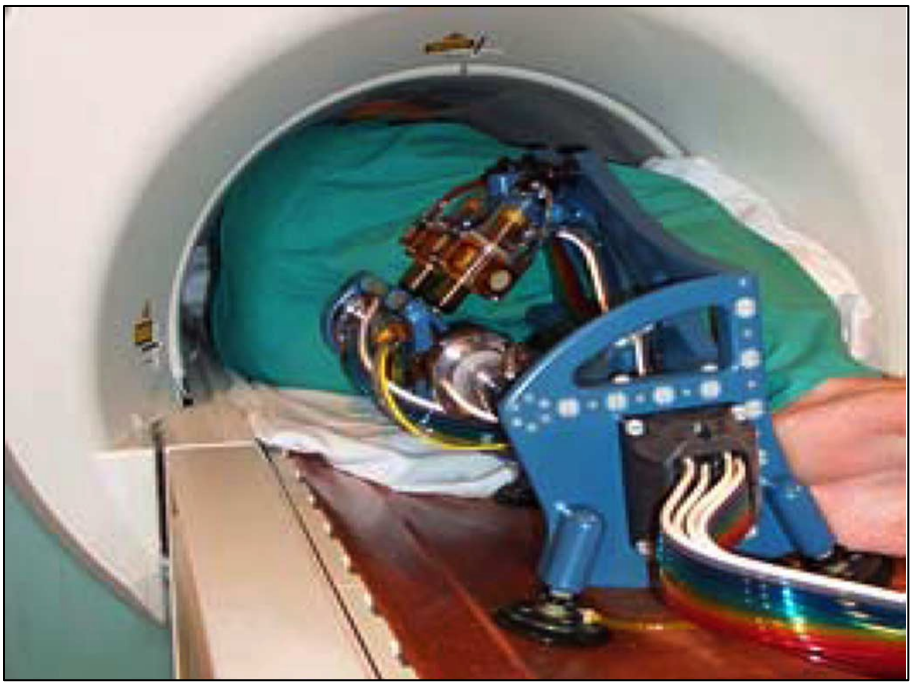

Figure 10: PneuStep Robotic System

It was determined that the implementation of a more versatile pneumatic stepping technology is possible. However, because the PneuStep was designed for use in diverse medical environments, and

because image guided intervention was the driving inspiration behind the development of the PRiSM, PneuStep may be considered the closest technology to that developed in this paper.

Methods

The design and analysis of the pneumatic motor detailed in this report consists of three main tasks. The first was the designing and manufacturing of the motor. After the motor was manufactured, a suite of software was developed to both actuate the motor and run the tests. Finally, tests were built to analyze the motor's performance.

Motor Design

Concept

The conceptualization of this pneumatic stepper motor was driven by a growing general interest in Image Guided Intervention (IGI). One limiting factor in the development of IGI technology is the lack of MRI-compatible actuators with suitable technical capabilities. While some such actuators exist (Johns Hopkins Medicine, 2005), this type of actuator is uncommon and, thus far, a topic of specific study.

The inspiration behind this motor design wasn't IMI. The concept was an idea that had been explored in a casual manner and it was only while attending a lecture by professor of Robotics and director of the AIM Lab at WPI (AIM Lab), Greg Fischer, that the potential of the design became apparent.

The motor functions using a phase principle. At its most basic level, a rack is driven by pistons that oscillate in phase, in a state of synchronous operation, with one another. The pistons are oriented such that their central axes are normal to the translational axis of the rack, see Figure 11.

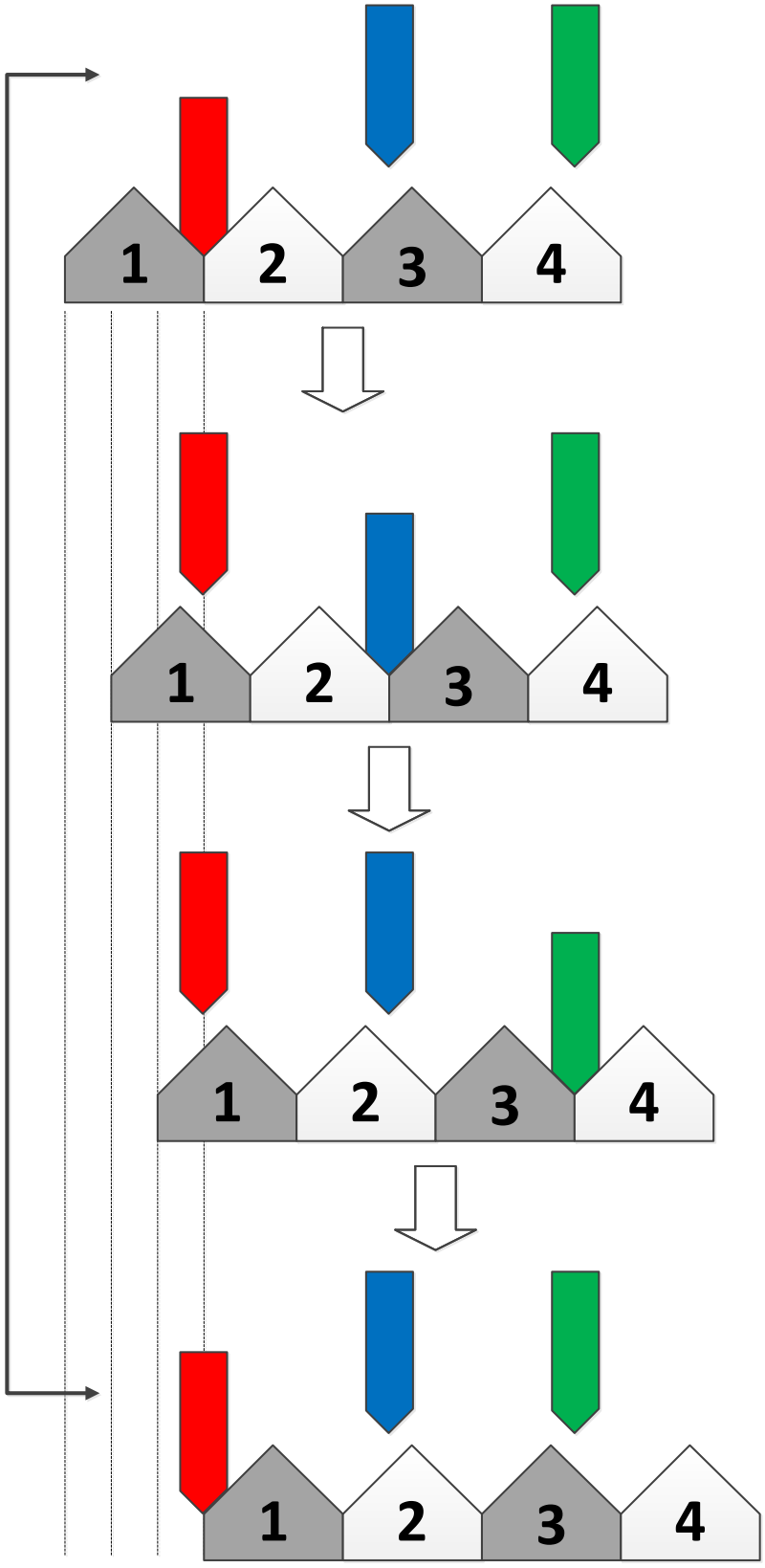

Figure 11: PRiSM Phase Principle

The rack model could be used to build a linear stepping actuator. This type of linear actuator is useful in some applications but the length of the driven component limits the actuation range. Due to the travel constraint, it was decided that a rotational model could prove to be more advantageous. A rotational model is very similar in principle to the linear model. If the linear rack were represented in a polar coordinate frame instead of a Cartesian one, the two ends of the rack would meet, creating one infinitely long rack. The pistons, now orientated normal to the rack and a radially spaced around a central drive axis, would turn this circular rack (gear). Figure 12 depicts the basic rotational model of the system.

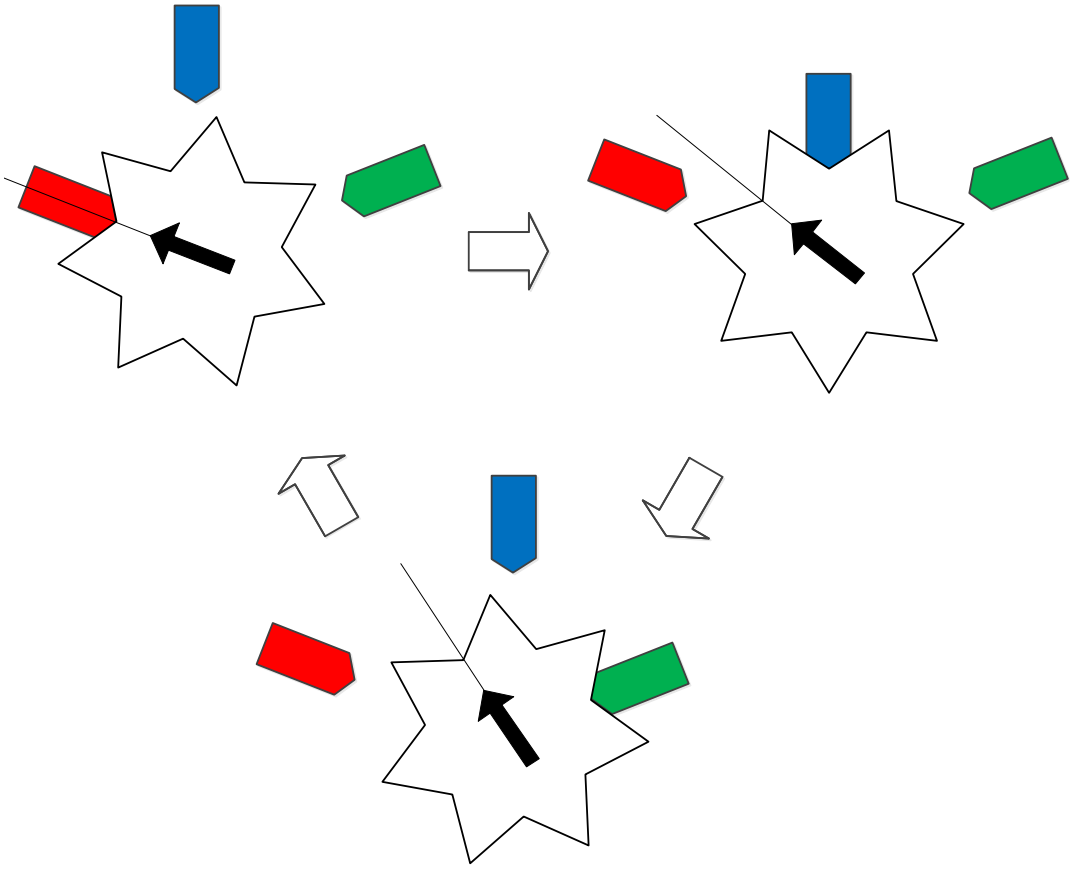

Figure 12: PRiSM Rotational Model

The design of the motor is driven by a number of variables including:

$$q = resolution\ (deg/step)$$
$$a = angle\ between\ drive\ teeth$$
$$n = number\ of\ teeth\ on\ the\ drive\ gear$$
$$D = number\ of\ driving\ pistons$$
$$R = outer\ radius\ of\ the\ drive\ gear$$
$$\mathrm{B} = internal\ angle\ of\ gear\ teeth$$

These variables can be determined based on the manufacturing capabilities available, the material used to fabricate the motor, the size of the motor, the available pressure, the actuation time of the driving solenoid valves, and a number of other factors. A redrawn model depicting these variables can be seen in Figure 13**.**

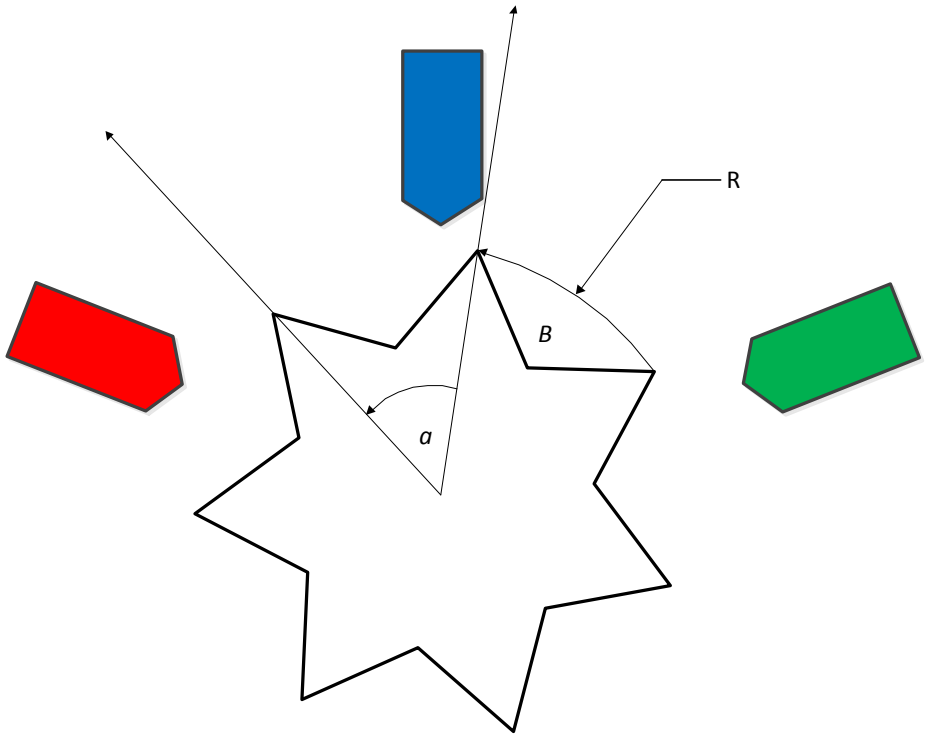

Figure 13: Demonstration of Dimensions

The motor must have three or more pistons because of the spacing relationships between the teeth and the pistons. If only two pistons are present, the second piston, when actuated, would make contact on the tip of one of the drive teeth. Aside from causing potential material damage, this interference would not generate any rotational torque or motion and would cause the motor to stall.

When designing the functional prototypes exhibited in this project, a principle factor was manufacturability. Due to the lack of special tooling available, the limited amount of stock material, the specific machines available, and the proof-of-concept nature of the project, the features in the motor revisions here are kept to an easily feasible machining level for an amateur machinist.

Motor Revisions

Revision 1

Before considerable time was invested in producing a fully functional model, a proof-of-concept was created. This proof-of-concept was built out of 6mm thick acrylic using a VLS 4.6, a laser-cutting tool (Universal Laser Systems, 2011). Figure 14 shows the assembled proof of concept.

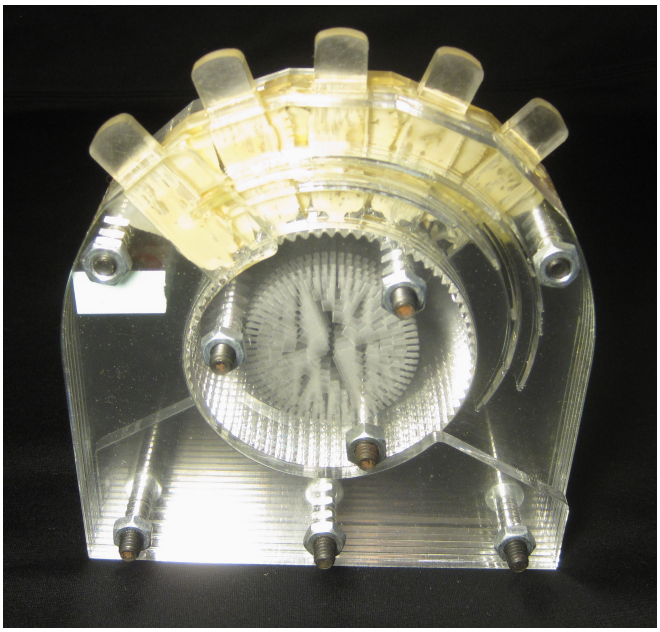

Figure 14: Proof of Concept (R1)

The pins along the top of the model could be pushed by hand causing them to engage the drive gear in the center. The driving geometric parameter for this model was:

$$q = 1^{\circ}$$

yielding 360 steps for one full revolution of the drive gear. The dimensions and angles of this model were chosen to be:

$$D = 5$$

because an odd number of pistons five or greater allows for the demonstration of a secondary principle; if D is greater than or equal to five, the pistons may be fired in an alternating sequence. In this sequence, every second piston is skipped and the resulting cycle, by piston number, would be 1, 3, 5, 2, 4. In this sequence, the drive gear achieves double the original rotational speed while maintaining the original torque.

$$c = 90°$$

c was chosen because a traditional milling tool has a 90° corner angle and, were a model to be manufactured using the same dimensions, this incident angle lends itself to ease of manufacturing.

Based on *q, c,* and D, *n* can be determined using the following equations:

$$n = 360/(qD)$$
$$n = 360/(1 * 5)$$
$$n = 72$$

Now, *n* and *c* are used to determine the size of the drive teeth. This size, when considered along with the drive gear material, acrylic, and the capabilities of the laser cutter (cut width of $5x10^{-3}$in) was used to qualitatively determine *R*, therefore:

$$R = 2.5in$$

The pistons in this case were replaced with spring-pins, lubricated with white lithium grease, which allowed the model to be driven by hand. The result was a working proof-of-concept. This model (considered revision 1) justified further development and initiated an iterative process of design and review.

Revision 2

Note: The decision to continue development of a fully functional prototype invited a new range of considerations including, but not limited to, overall size, weight, material composition, desired resolution, desired speed of operation, type of drive solenoids, size of pneumatic tubing to use, operating pressure, output shaft length and diameter, MRI compatibility along with many others. The scope of the project didn't allow for the thorough exploration of every variable's impact on motor performance so assumptions were made regarding certain aspects of the construction and requirements. These assumptions will be stated in the process of design documentation.

The first decision was made with regard to the motive-force, which would drive the pistons. This force could be provided by a hydraulic system or by a pneumatic system. These two were the only two options considered because the goal was total MRI compatibility. Some actuators exist which are MRI compatible while not in operation such as a ceramic motor (Nanomotion), but these actuators require electricity to operate and the induced magnetic field created by these electrical circuits, while not dangerous, can distort the images produced by the MRI machine and were therefore eliminated from consideration.

Hydraulic systems provide an incompressible force, which is generally larger in magnitude than that of pneumatic systems. Hydraulic systems generally can be controlled to reach a number of positions whereas pneumatic systems are typically two-phase. Hydraulic systems require a sealed system and any leakage resulting from machining tolerances, wear, or part failure, leads to total system failure. Lastly, considering the medical nature of the application, sterile air supplies are available in a hospital, but a hydraulic system would not be commonly available. After weighing the characteristics of hydraulic and pneumatic systems, the decision was made to utilize a pneumatic system for the duration of this project.

It was thought that a logical first step would be to design a fully functional motor using similar geometry to that which was used for revision 1 (R1). This was because it was already shown to work and it logically followed that if it worked by hand then the greater force and machining precision used in a fully functional version would work as well.

Working on a limited budget, the first revision was limited to stock material readily available to the project. In particular, 1" thick acrylic sheet was available for the housing material, the 6mm acrylic used for revision 1 would be used for the face and back plates, and 6061 T6 aluminum would be used for the drive gear and pistons.

Once the decision to use a pneumatic system was made, the first consideration was for the design of the pistons. The pistons each have a chiseled tip and the flat side of the tip makes contact with the flat side of the gear teeth. The motor needed the ability to keep the pistons from rotating about their central axes. This need, combined with the material thickness constraint, led to the design of a square-headed piston. Pistons with non-circular heads are not typical due to problems encountered when trying to seal the pistons.

The next consideration was for the interaction between the pistons and the drive gear, defined by incident angle, β, which has an effect on the output force of the motor and determines the actuation distance required from each piston. Although any angle would work, the smaller the angle, the greater the mechanical advantage that is achieved between the piston and the drive gear. When looking ahead to the manufacturing of the motor, it was recognized that the only two practical incident angles that could be created were 60 and 90 degrees. This incident angle was used to determine both the angle of the teeth on the drive gear and the angle of the chisel-tip on each piston, because the two angles are equal.

The next consideration was for the drive gear. Based on limited manufacturing experience, the process devised to cut the drive gear was to make tooling passes parallel to the central axis of the drive gear, and spaced radially around the circumference. The tool used would need the same tip angle as the desired incident angle (60 degrees in this case). A tooling search led to the purchase of a 60-degree, four flute, .25” chamfer end mill from McMaster-Carr (McMaster-Carr). Using the dimensions of the tool and an approximation of its capabilities, the angle between the teeth was chosen and consequently, the number of teeth.

$$\alpha = 10^\circ$$
$$n = 360/\alpha$$
$$n = 36$$

The drive gear would be mounted in a housing which fixed it axially and spatially using bushings pressed into the outer housing and a front faceplate. A series of assembled housing rings were designed to allow for the integration of piston springs and pneumatic fittings. These rings were chosen instead of a solid housing due to machining and material constraints. Each ring had a locating feature that aligned it rotationally with the rest of the rings. This was to allow for ease of assembly. The outer housing shell

had motor mount holes so that the motor could be mounted easily to a fixture or other mechanism. A final image showing PRiSM R2 can be seen in Figure 15.

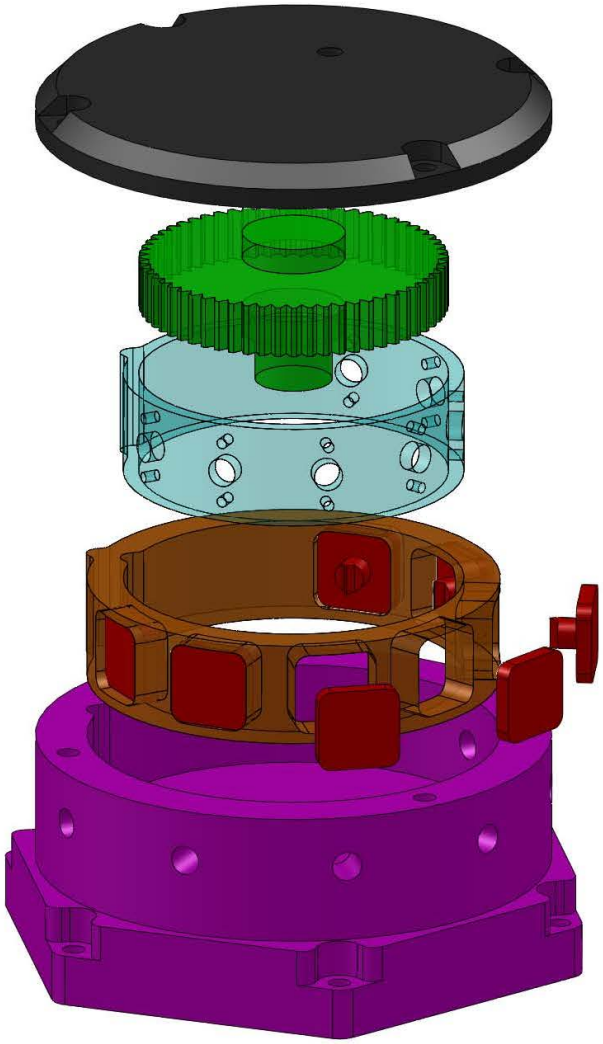

Figure 15: Solid Works Model of R2

Revision 3

R3 incorporated one main change from R2. The pistons were changed from a square shape to an elliptical shape. This was done in order to more closely resemble standard pneumatic components, which are circular in shape. The ellipse was dimensioned with manufacturability in mind (considering the minimum internal radius and minimum wall thickness).

A second minor change was the elimination of the spring retaining ring. This was done to reduce the number of machined parts and to improve the overall robustness of the motor.

R3 was manufactured from acrylic blocks. The machining tolerances, without enough material to re-machine parts, were poor (+/- .020”) due to thermal expansion. The slip-fits of the pistons required adjustment. Steel springs were used in place of MRI-compatible springs because of the availability of common springs for the purpose of function testing.

One problem that became immediately evident was lubrication. It was assumed that a slip-fit would not require lubrication. As it turned out, the interacting wear surfaces between the pistons and the cylinder walls were binding together over time. A silicone lubricant was used as a short-term solution, but it was evident that a longer-term solution was needed.

Figure 16 below shows a rendered SolidWorks model of R3. Figure 17 shows a picture of the constructed motor.

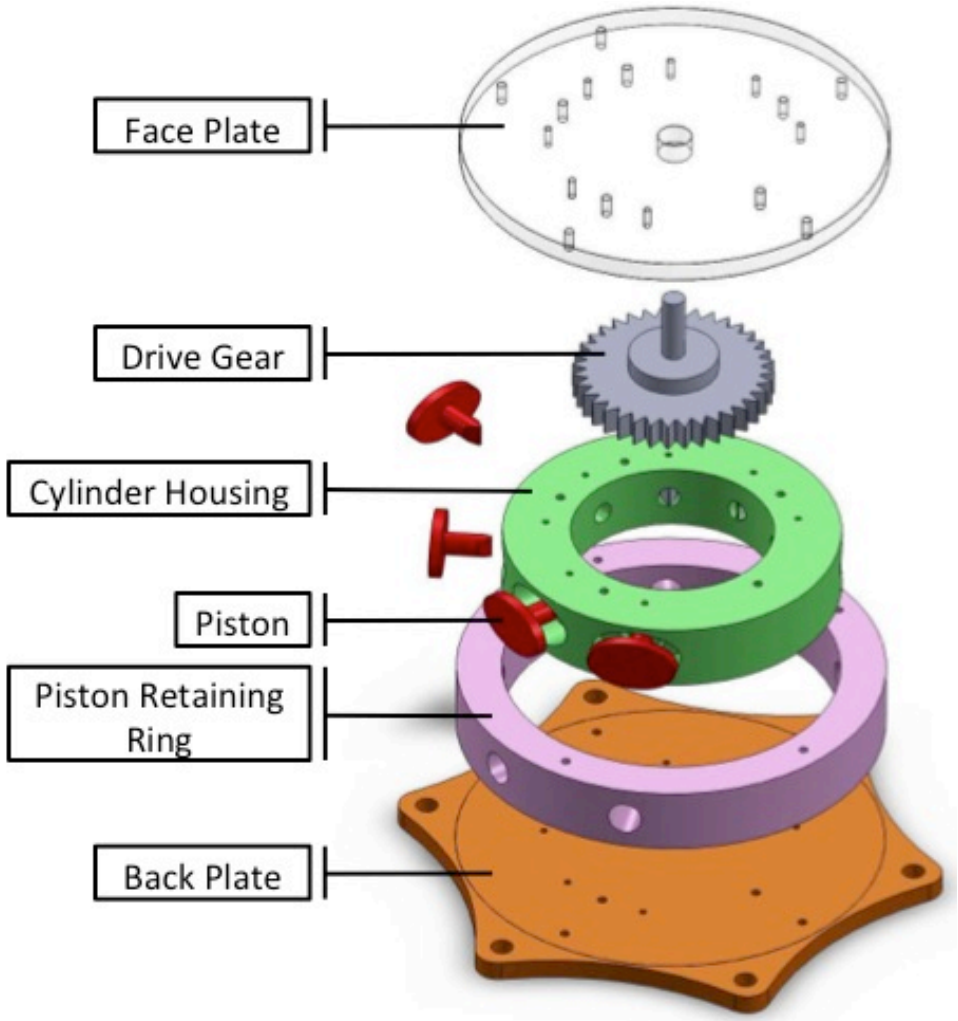

Figure 16: R3 Annotated Exploded View

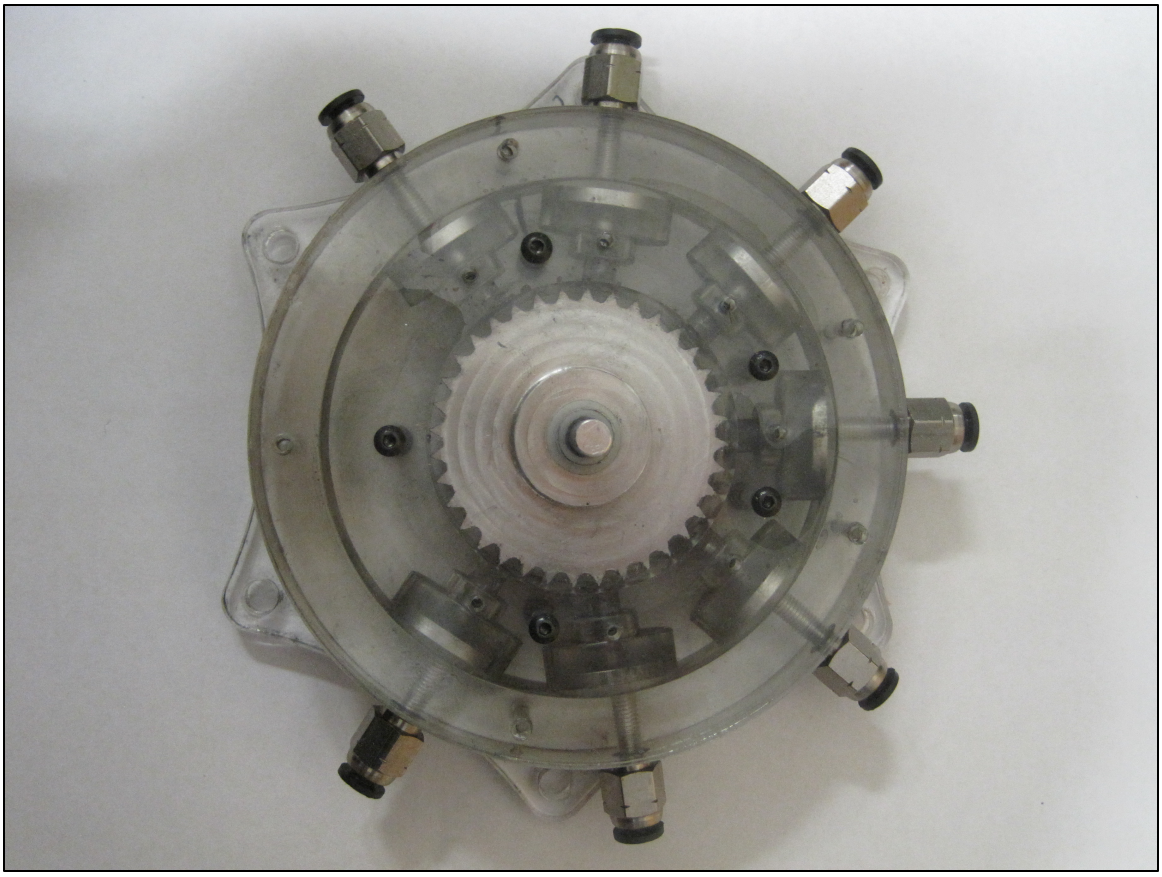

Figure 17: Construct R3 Motor

Revision 4

The differences between R3 and R4 will be explained in the order in which they were implemented. First, the housing material was reconsidered. Originally, acrylic was chosen for the housing material due to its availability. There was enough of this material available to the project to make manufacturing the housing feasible without acquiring more material. After R3 was shown to work, and the running hours of the motor increased, a binding problem was discovered. It is assumed, although not confirmed, that the acrylic housing was wearing and the material worn off the housing was causing the pistons to bind. It was at this point that the need for a new material was identified.

With feasibility in mind, a self-lubricating plastic with a high machinability rating and a very high wear-resistance was sought. After speaking with an engineer at Plastic Unlimited Inc. (Plastics Unlimited Inc., 2011) in Worcester, MA, ultra-high molecular-weight polyethylene (UHMW-PE) was determined to be a suitable material. Further research into UHMW-PE yielded that the material exhibits the high abrasion-resistance, high machinability, and self-lubrication desired.

Another lesson learned from R3 is that the concentric ring construction made assembly a laborious and painstaking process. It was obvious that a sealing method that allowed for access to single pistons would make assembly easier. As a result, the housing changed to a seven-sided polygon shape, shown in Figure 18.

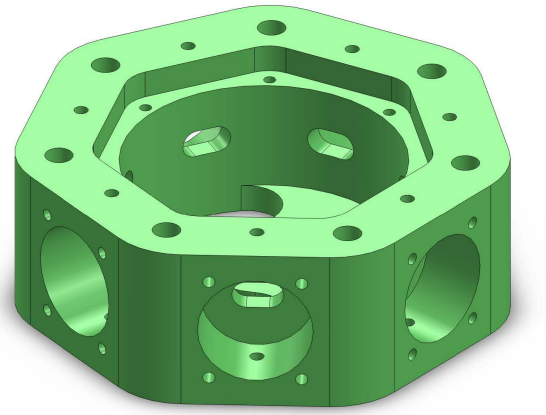

Figure 18: R4 Solid-Body Housing

Each cylinder would be sealed with its own sealing plate and custom-cut gasket. The sealing plate would be attached to the housing using fasteners with the same thread as those used in R3, but would be substituted for thumbscrews to allow for tool-free assembly.

The most prominent observation from R3 was that a significant amount of air was leaking around the piston heads. Since the decision had been made to leave the pistons sealed with merely a press-fit, and because the machining tolerances attained were pretty large, a large volume of air was escaping through the low-pressure exhaust holes. It was already noted during the design phase of R2 that circular would allow for the use of O-rings and that this option was not chosen due to the presence of an unlimited air supply. The leakage noticed in R3 forced the reconsideration of this design characteristic. In R4, the pistons would have round heads to accommodate O-rings, if necessary. Making the heads circular reintroduced the need for a feature that prevented the pistons from rotating about their central axes. To do this, the push rod of each piston was made into an ellipse.

The diameter of the drive gear was increased to afford more space for a larger drive shaft. The new drive shaft would be .375” in diameter in contrast to the original drive shaft’s diameter of .25”. The newer diameter made it easier to utilize a longer drive shaft. It was thought that a longer drive shaft would make the design of testing fixtures easier. Another changed feature of the drive gear (and pistons as a result), was a new incident angle of

$$c = 90°$$

While manufacturing R3, the chamfer end mill broke. A new manufacturing method was chosen which would require the use of a square end mill with a corner angle of 90 degrees. This resulted in an incident angle of 90 degrees.

R4 was manufactured but never functioned due to problems with tolerances of the pistons and the housing. It was discovered that machining plastics using traditional means leads to a very large amount of thermal expansion. Perfectly round cylinders could not be manufactured; therefore the slip-fit of the pistons was leading to an unacceptable volume of air leakage around the piston head

Revision 5

The driving difference between R4 and R5 stemmed from the need for a better seal between the pistons and the piston housing. It was originally assumed that, because the motors would be run off an infinite air supply, a small amount of leakage could be tolerated. Due to thermal expansion during manufacturing, the desired unsealed slip-fit was considered infeasible and new solutions were explored. An O-ring was added to a groove in the piston. Wanting to keep the friction between the piston and the housing low, the O-ring was not utilized in the typical fashion. In this design, the O-ring groove was manufactured to be deeper, lowering the contact area and pressure. The second distinguishing difference was that the groove was made wider than the O-ring. The desired effect was that the O-ring would roll in the groove between the piston and the piston housing, changing the friction it caused from a sliding friction to a rolling friction, which would be lower, and still maintaining the desired seal. Figure 19 shows the piston with the O-ring already mounted in its rolling groove.

Figure 19: R5 Piston With "Rolling O-Ring Groove"

Initial qualitative tests showed that the new sealed pistons provided more force than the original pistons. R5 used the same Ultem™ plastic springs used in R4 (Lee Spring, 2011). The full springs utilized are shown in Figure 20 and its data sheet can be found in Appendix J.

Figure 20: Ultem™ Piston Spring from Lee Spring

As a result of adding the O-ring, the piston was elongated from the pistons used in R4. The housing needed to be made larger to accommodate the increased size of the pistons. The new and final housing can be seen in Figure 21, Figure 22, and Figure 23.

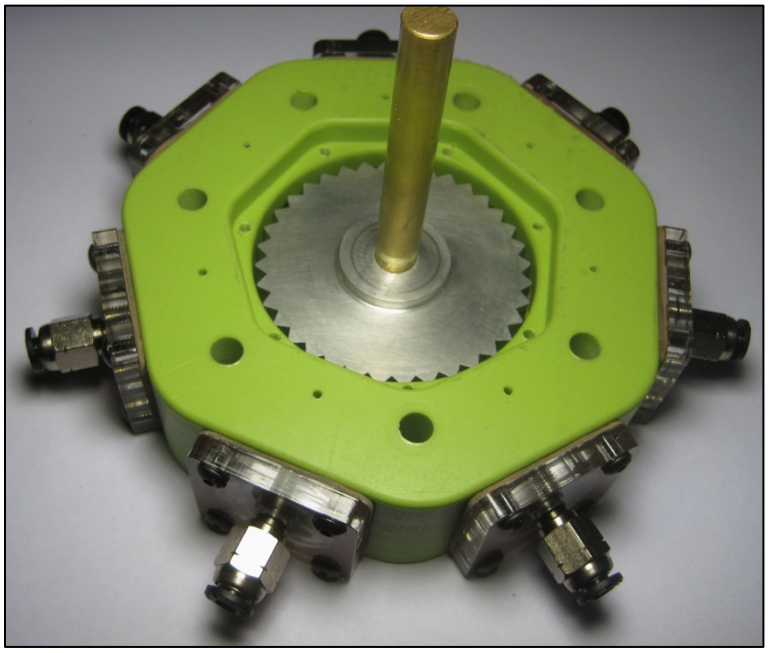

Figure 21: R5 With Face Plate Removed

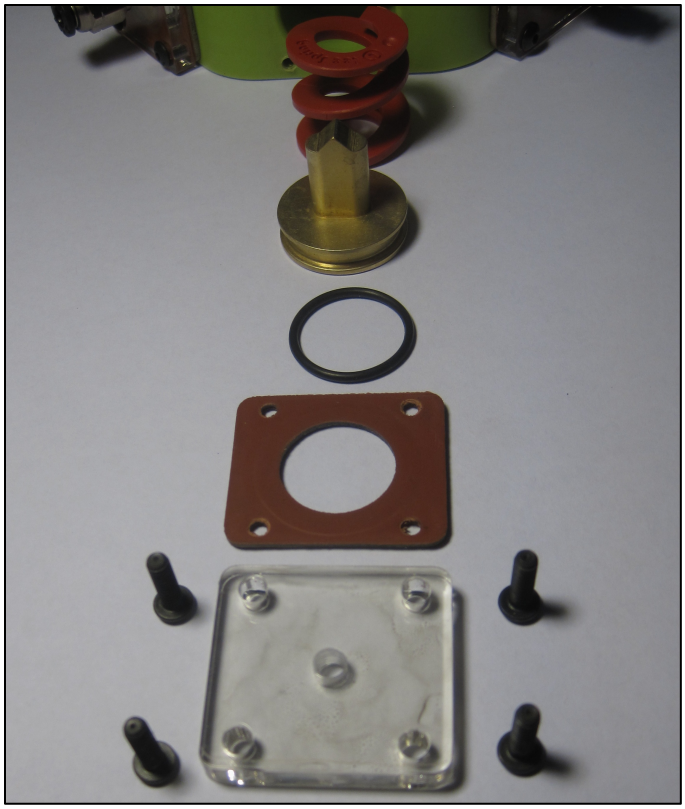

Figure 22: R5 Piston Assembly Layout

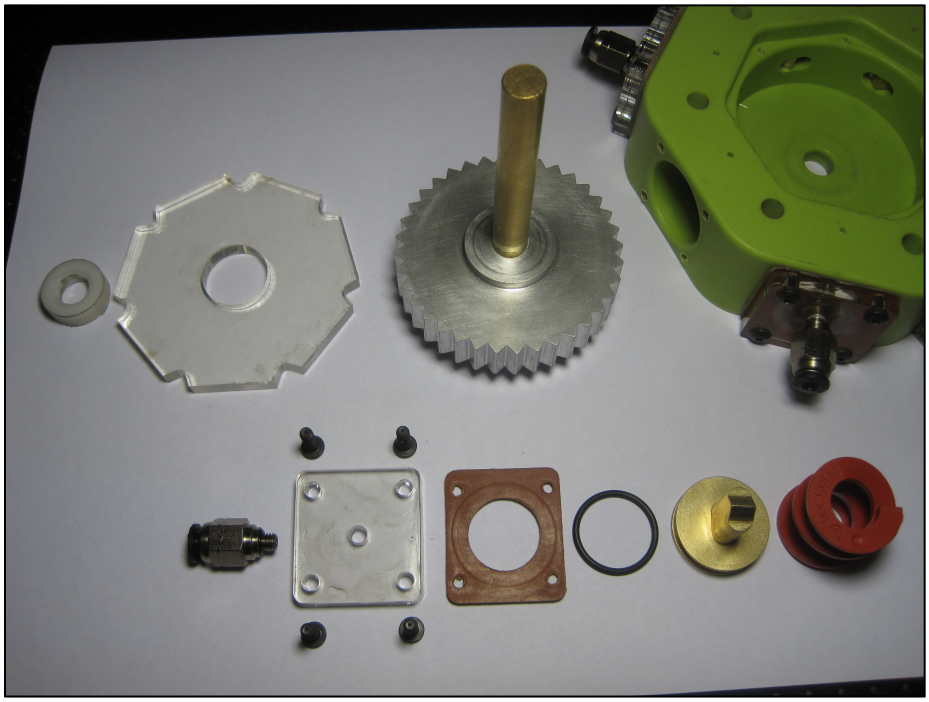

Figure 23: R5 Disassembled

Propagation Delay Testing

To control motor speed, it is necessary to obtain individual cylinder response delays. This delay consists of two parts. The first is the propagation delay, and the second is the delay resulting from the time necessary to pressurize the piston volume. Cylinder response timing is necessary to achieve accurate motor control. Because this test could be run without the motor, this was the first test to be conducted. The propagation delay test measured the time delay between the firing of a solenoid and the point at which an entire length of hose reached full pressure. In this section important components of the experiment will be laid out and the final experiment design will be explained in great detail.

Pressure Sensor

The air pressure in this experiment was set to 80PSI. To measure this value the MSP-300-250-P-2-N-1 pressure sensor was chosen. It operates from 0-250 psi with a 0-100mV output and can be seen in Figure 24. The full datasheet can be seen in Appendix A.

Figure 24: MSP-300-250-P-2-N-1 Pressure Sensor

Differential Amplifier Circuit

The output from the pressure sensor falls within a 0-100mV range, which must be scaled, in order to be read by the cRIO. In addition, the measured value is actually the difference between two outputs from the pressure sensor. An operational amplifier circuit was made to obtain and scale this difference. The circuit was constructed using the LM324 single ended op-amp. The single ended amplifier was selected so a negative power supply would not be necessary to run the circuit. The

datasheet for the LM324 and its pin outputs can be found in Appendix B. Figure 25 contains a diagram of the operational amplifier circuit used.

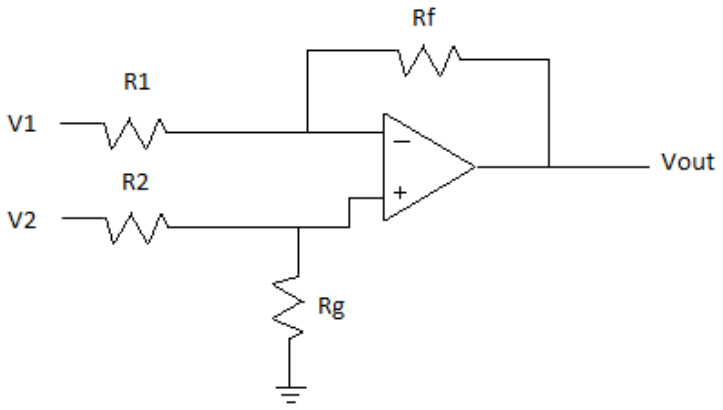

Figure 25: Differential Op Amp

The equation below shows the transfer function of the differential operational amplifier circuit. This equation assumes the $R_f = R_g$ and $R_1 = R_2$.

$$V_{out} = \frac{R_f}{R_1}(V_2 - V_1)$$

For this experiment a gain of 100, (R_f/R_1 =100), was selected. The resistor values used in the circuit are listed in Table 1. The actual measured values of the resistors are also shown. This allows for the resistors 5% tolerance to be calculated as error. With the actual measured values the gain becomes 99.4 instead of 100, which was used in all further calculations.

	R_f (KΩ)	R_g (KΩ)	R_1 (KΩ)	R_2 (KΩ)
Desired	100.0	100.0	1.000	1.000
Actual	98.2	99.7	0.988	0.986

Table 1: Resistor Values (Desired vs. Actual)

The LM324 is connected to the pressure sensor. The green wire is the positive output of the pressure sensor connected to V2 and the white wire is the negative output of the pressure sensor connected to V1. The red and black wires of the pressure sensor are connected to positive 5v and ground respectively. The full explanation for how to construct the circuit can be found in Appendix C.

With the pressure sensor ready to read values, calibration data was collected using an oscilloscope and a variable air pressure source. These measurements were taken at 80, 70, 60, and 40 psi. Table 2 has the corresponding output voltages for the measured pressures.

Pressure (psi)	V_{out} (V)
80	1.24
70	1.12
60	1.00
40	0.76

Table 2: Calibration psi input vs. voltage output

This table demonstrates that the output of the sensor is linear and that 0.0155 Volts represents 1 psi. These calculations are done by dividing each pressure by the measured V_{out}. Using this value the output of the differential amplifier circuit can be simply divided by .0155 Volts/psi to give the pressure of the system. Table 2 shows that when the pressure is 80 PSI, output voltage reaches 1.24 V.

Solenoid and Pneumatic Tubing

The operation of our actuator design requires air pressure to be applied to several pistons. To manage this air flow, a twenty-four solenoid manifold was chosen. The solenoids in this manifold are NJV3333. Appendix F has the datasheet for the NJV3333. Figure 26 shows a picture of the solenoid manifold. For this experiment only two solenoids of the twenty-four were used. One was connected to the pressure sensor for measurements and the other was used to release pressure within the measurement line.

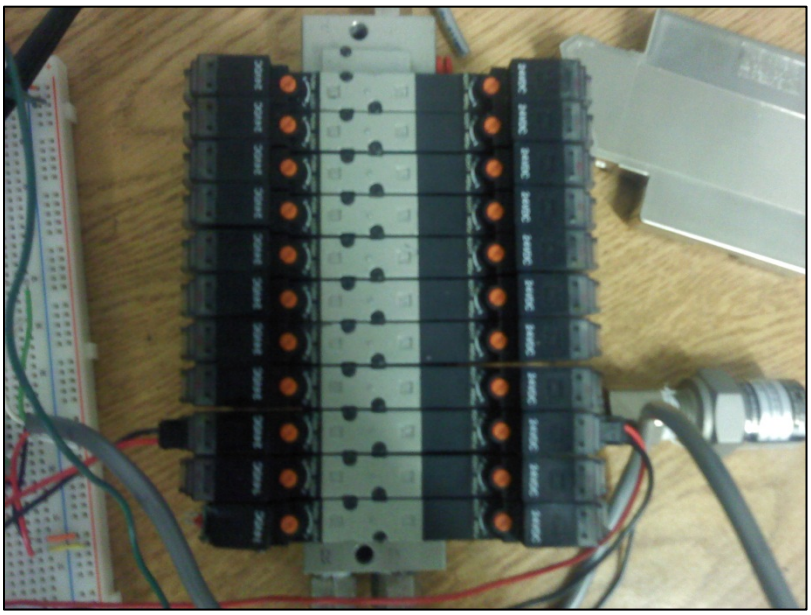

Figure 26: Solenoid Manifold

The delivery of air to our actuator pistons requires pneumatic tubing. For this experiment 1/4" and 5/32" diameter pneumatic tubing were selected. To decide upon optimal length for our application the lengths of 5', 10', and 15' was tested for each diameter. One measurement of the pressure sensor connected directly to solenoid will be used to estimate solenoid delay.

National Instruments cRIO

To run this experiment the National Instruments cRIO was used. The cRIO both actuated the solenoids and read the output of the pressure sensor. More information about the software used in this test is in the Software Development section of the methodology. A full step by step process for this experiment is in Appendix C.

Motor Speed Testing

The motor speed testing was the first test performed on the actuator itself. The goal of this test was to measure the speed at which the motor operates based on the frequency at which the pistons are fired. Along with testing speed, this test allowed for the observation of motor consistency.

Blast Shield

For the initial function, a blast shield was constructed to insure safety in the event of an unanticipated incident. The blast shield was created from a 2 foot by 3 foot plastic container. The inside was insulated with foam and 1/4" wood that minimized the sound of the actuator while also offering additional protection. The lid of the container had a square piece replaced with Plexiglas for observation purposes. Figure 27 shows the blast shield with actuator inside and the top removed.

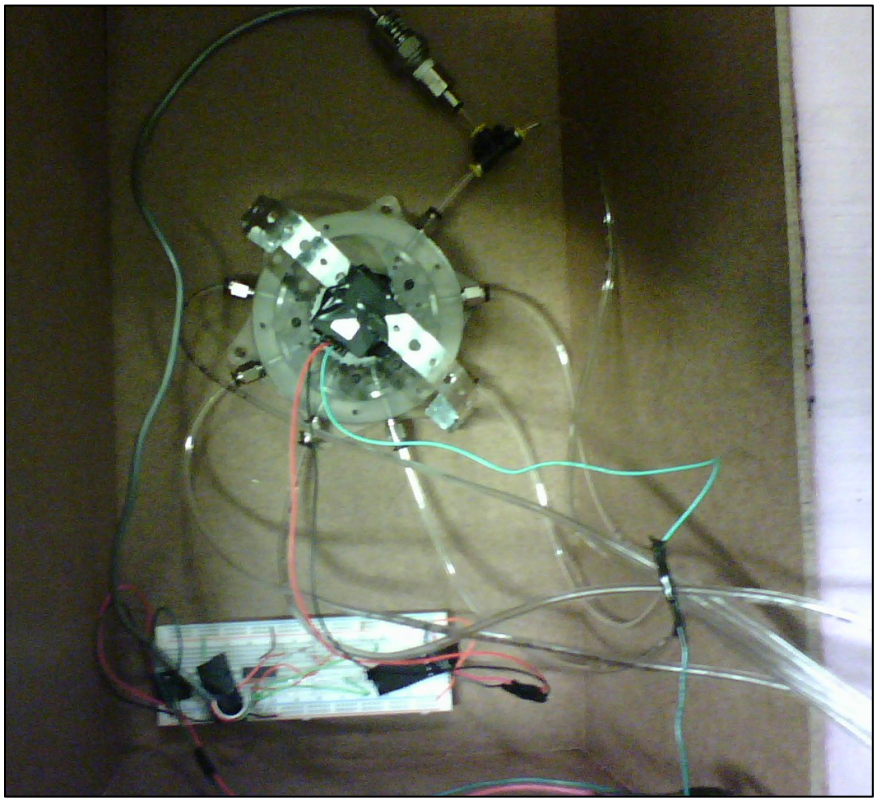

Figure 27: Blast Shield with Motor

Potentiometer

A potentiometer was used to measure the motor's shaft position. While the potentiometer did not measure the total number of degrees turned, it did keep track of relative position of the shaft. The model of potentiometer used for this experiment was a Vishay Model 601-1045, for the datasheet refer to Appendix D. This model of potentiometer returns an analog voltage signal from roughly .10V to 4.5V.

This voltage range corresponds directly to a 0 to 360 degree range. After the encoder spins past 360 degrees with the output of 4.5,V it resets back to 0 with the output of 0.10V. The power required for this potentiometer is 5V and the output is connected directly to the cRIO analog input. Figure 28 shows the encoder attached to the motor shaft with a rubber coupler. It is held in place with a metal bracket and screws that secure it and the motor to the blast shield.

Figure 28: Actuator Speed Test Set-Up

Actuator Preferences

The speed testing required the actuator to be operated at different frequencies. The frequencies of operation that were picked to test the motor's speed capabilities were 500ms, 250ms, 100ms, 60ms, and 40ms. These frequencies were all tested for 100 two-minute tests. In addition, tests of 100 revolutions were run at 200ms and 300ms periods to more accurately test open-loop functionality

National Instruments cRIO

The program used to run this test was called Run Speed Test.vi. This program is detailed in Appendix E.

Torque Testing

In addition to determining the optimal speed the at which the actuator can operate, it is crucial to measure its torque output. If the motor can apply only a minimal force, it greatly reduces the applications in which it can be effective. The test in this section will measure the motor's maximum torque output. This value can then be used as a threshold to determine possible applications.

Torque testing was the final test to be performed on the actuator. This test provided the maximum torque (in N*mm) that the actuator could achieve at 60 psi. To require less weight in the test, a torque disk was machined. The torque disk had a radius of 63.5mm and can be seen in Figure 29. A Kevlar string was wrapped around the disk and secured so that it could be used to attach weights. The test consisted of running the motor at an arbitrary speed while continuously adding weights to the string until the motor stalled. The heaviest weight lifted by the motor while still functioning properly is used to determine the torque output. The values used to calculate torque can be seen illustrated in Figure 29. The force shown is the tension that the motor applies to the string as it rotates. This force is multiplied by the radius to calculate the torque output.

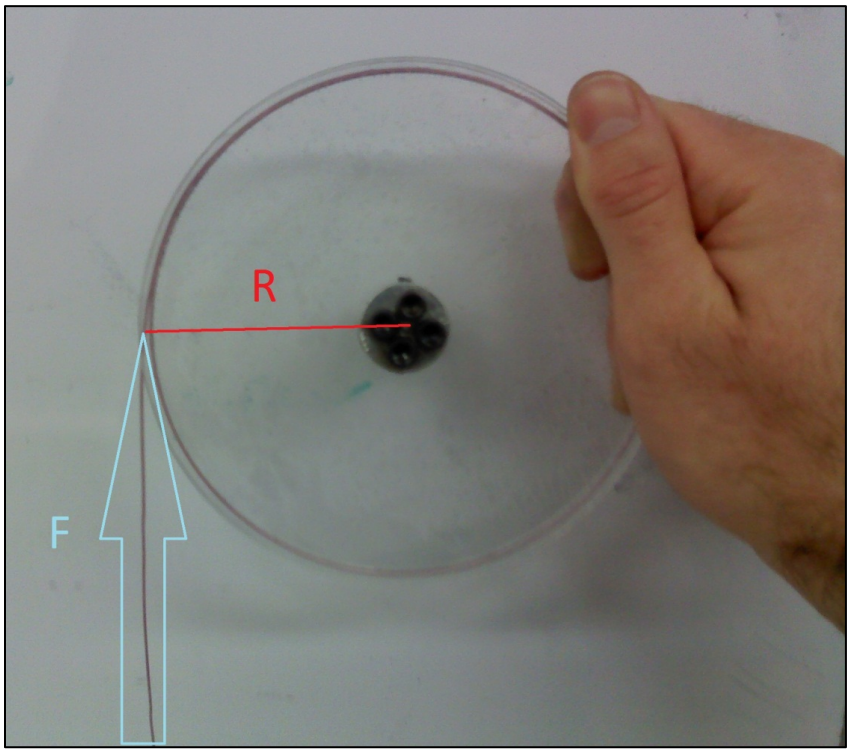

Figure 29: Torque disk with component drawings

Software Development

Choosing the Controller

The motor designed for this project is pneumatically driven. To make sure that the solenoid is running properly there must be a controller. The controller's job is to send digital signals to the solenoids in order to run the motor properly. To be able to do this well, a controller had to meet several specifications. First, the controller had to have a minimum of 14 different outputs that send a digital signal that can switch the 24V solenoids being used. Fourteen was the minimum number used because it is the number needed to run two motors simultaneously. (For demonstration purposes, two motors will be utilized to drive a linkage.) Next, the system should be able to take inputs so that sensors can be used. The controller also needed to be capable of highly accurate timing, and ideally being able to time multiple different tasks simultaneously. With all of these considerations made, the cRIO 9704 was selected.

Learning LabVIEW

In order to have the cRIO run the motor, the cRIO was connected to a PC. The cRIO and PC communicated through an Ethernet connection. Using National Instruments' Measurement & Automation Explorer software, the connection was set up, and LabVIEW was automatically configured to recognize the cRIO. With the cRIO working, testing its basic capabilities was the next step.

The controller software was developed through a process of iterative design while gaining familiarity with LabVIEW. Each iteration of the software incorporated additional functionality until the desired goal of controlling the motor was achieved. The first program simply turned on the cRIO LED. Because LabVIEW turns on the LED the same way it turns on its digital output, this initial program verified that the cRIO could turn on and off its outputs.

The second program turned on and off the LED in a timed loop. Accurate timing is necessary to create the desired behavior needed from the motor. Within this program, the first loop created on the cRIO had periods and duty cycles that could be determined by the user. The LED would correspondingly turn off and on using the specified period and duty cycle. The loops made in this program ended up being similar in style to the loops made in subsequent programs.

The final piece of code made before the testing began was a simple solenoid switch, Figure 30.

Figure 30: Solenoid Switch GUI and Solenoid Switch Block Diagram

The code itself just turns off and on the Digital Output on module 7. This module does not actually output any voltage; instead it controls a switch in effectively a circuit diagram like the one shown in Figure 31.

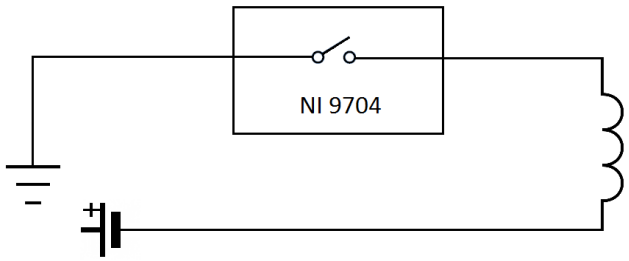

Figure 31: NI 9704 connected to solenoid Circuit Diagram

This means that an independent power source is needed to run the solenoid. It takes an input of 24V. For testing this code, a GPS-3303 Laboratory DC Power Supply was used. With the program running and the solenoid set up with power, the user needs only to press the Mod 7/DO0 button on the GUI to turn on and off the solenoid. This program does not have a large amount of functionality, but it proved to be useful in proving that the cRIO was successfully turning on and off the solenoid with a delay small enough to be imperceptible by human senses.

Developing Propagation Delay Testing Software

The testing software accomplished three tasks. First was running the test and collecting the data through the cRIO. This was achieved through a timing loop that switched the solenoids on and off according to a pre-determined loop, and retrieving the data from the analog inputs at a sampling rate of 1000 samples per second. This was an extension of programs mentioned earlier.

The second task was writing the data to a file using the host computer. LabVIEW has a built-in function that writes an array into a spreadsheet, so this task was accomplished by using the built-in function and formatting the data being handled into an array.

The final task was enacting an information transfer between the host and the cRIO. To accomplish this task, three different architectures were built and tested.

The first architecture was synchronous data transfer. The concept behind this architecture is to synchronize the host computer and the cRIO, so the host collects the data from the cRIO as soon as the data is acquired. This architecture would have run quickly, and does not require much data packaging on the cRIO side. The downside was that the host computer could not be timed consistently. The tools offered in LabVIEW are not sufficient to provide accurate timing on the host computer. The end result is that this architecture could not be successfully implemented. The tests all resulted in the data transfer having large sections of error when the computer tried to collect data when the cRIO was not producing any, or collecting at a faster rate than the cRIO was running. With these results the architecture was deemed not useful for further exploration.

The second architecture tested was interrupt driven synchronous data transfer. This works in a similar manner to the first architecture with the exception that the machines were synchronized through interrupts. The upsides were the same as above. However, efforts to transmit interrupts from the cRIO to the host computer were unsuccessful. Through process of learning how to set up those interrupts, another possibility for data transfer was discovered.

The third and ultimately chosen architecture was FIFO asynchronous data transfer. Here FIFO stands for First in, First out, or a queue. This works through the cRIO sending the data it collects to a buffer, where it waits until the host collects it. This was implemented through the LabVIEW FIFO block, and creating a FIFO object on the cRIO. The upside to this architecture is that the host and the computer do not need to be synchronized too closely. If not synchronized closely enough, there is a potential for data to be overwritten if the host waits too long to collect the data. In testing there appeared no significant downsides in comparison to the other architectures tested. In addition, it was the only architecture that successfully transferred data. For primarily that reason it was chosen as the data transfer architecture.

These two Virtual Interfaces (VI) were used together to run the propagation tests. A host VI started the cRIO VI which ran the test. As the cRIO VI gathered data from the Analog Inputs, the host VI retrieved the data through the FIFO. The data was then saved to a spreadsheet.

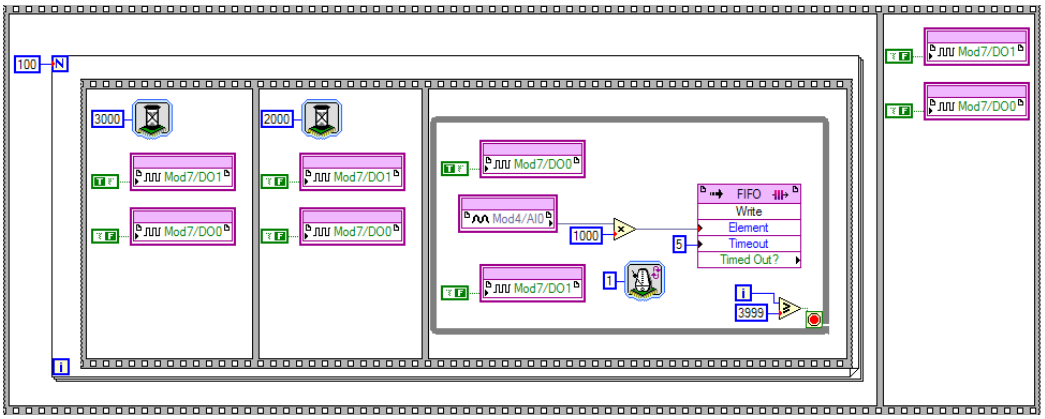

Figure 32: Propagation Testing cRIO Block Diagram

Figure 32 shows the code that the cRIO ran for the propagation tests. The flow of the program is dictated by the sequence frames (these are the containers which look like movie frames), which allow for one section of code to be run before another starts. There are two of these in this code. The most external one has two frames. The first one runs the test. The second turns off all of the outputs after the test has been completed. The reason for turning off all of the outputs is that the cRIO leaves on all digital outputs if they are not explicitly turned off. The actual test is inside the for-loop in the first frame. The sequence frame inside the for-loop performs the following sequence:

1. Empty the air from the main testing line by opening a second valve with the first turned off. This is done for three seconds.
2. Turn off the second valve. This is done for two seconds.
3. The main valve is turned on and the pressure sensor is polled once a millisecond, and that data is sent to the FIFO. This is done for four seconds.

That loop is repeated one hundred times, ending with 100 tests being run. Ultimately 400,000 data points are collected for each iteration of this program. This code ran on the cRIO. Figure 33 illustrates the code that ran on the Host Computer.

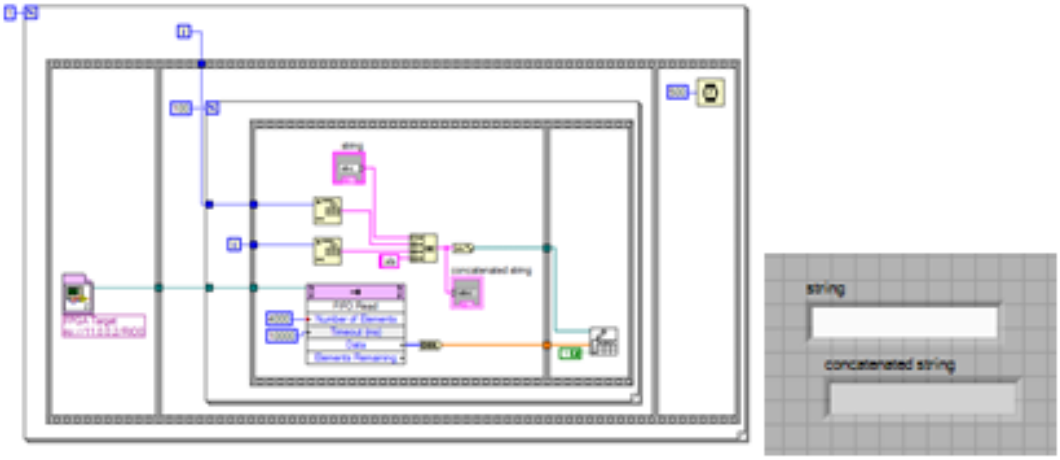

Figure 33: Run Test for Propagation GUI and Run Test for Propagation Block Diagram

This VI also used a sequence frame. The sequence frame does the following:

1. The Propagation VI is run on the cRIO
2. The data is collected for all one hundred tests through the cRIO.
3. There is a half second delay between iterations of the program is the for-loop is set to loop more than one time.

The data collected in frame two is saved to the host computer by being written to a spreadsheet file. The location of these spreadsheets is specified in the string control in the GUI. It is named with a .xls file extension so that Excel will be able to recognize it easily. The spreadsheets are numbered namexyy.xls, where x is the counter in the outer for-loop, and yy is the number in the inner for-loop. This creates files that are easy to separate by the order they were run. This code ran successfully and was able to collect the data from the propagation test to be analyzed. This was the only test that was run without the motor. The next task was creating a controller for the motor.

Software to Run the Motor

A simple program was developed to provide accurate control of the motor's pneumatic cylinder actuations. The program utilized two user-specified timing parameters. The first parameter controlled the amount of time pressure was supplied to each piston. The second parameter controlled the delay between pistons being pressurized. The interaction between these parameters was used to create overlapping piston actuations.

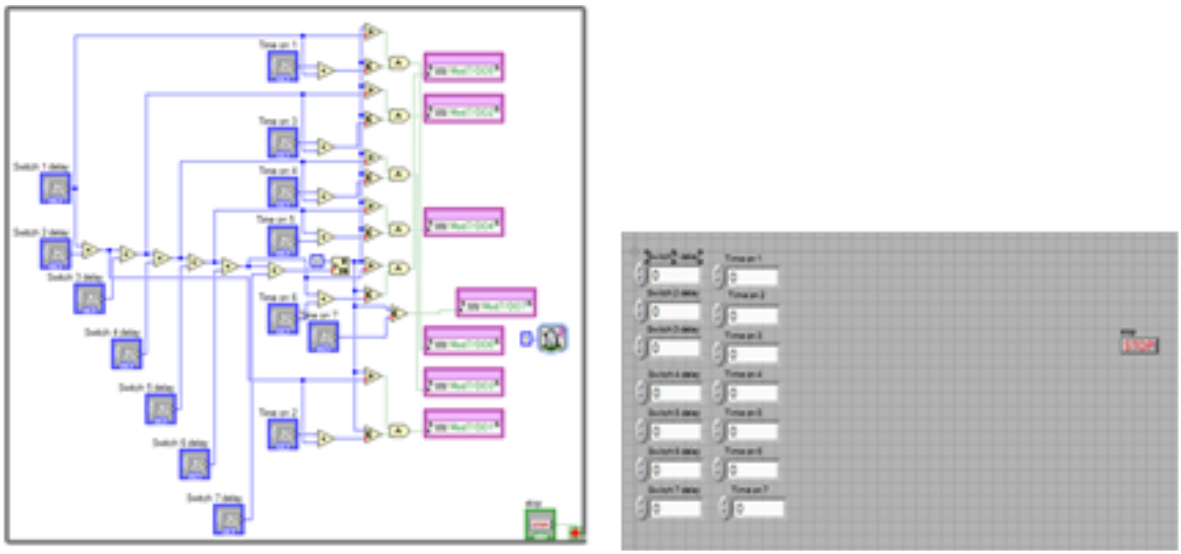

Figure 34: GUI for Running Motor GUI and GUI for Running Motor Block Diagram

The block diagram in Figure 34 illustrates the overall program code, and is simply a large for-loop with many checks to determine which solenoids should be on and which should be off. This requires a significant number of checks so that control loops can be made where multiple solenoids are on at the same time. In simple terms, it calculates the period of one loop, determines at what times within that one period the solenoids should be turned on, and then proceeds to loop through this endlessly. The GUI allows the user to specify the parameters that drive the motor. In practice the values entered into different solenoids were always identical, but the program was flexible enough to accommodate varying values. This code was the first used to run the motor and verify that it was working properly. While no hard data was collected, this confirmed that the architecture of the program would be successful in running the motor.

To make controlling the motor slightly easier for the user, a program that controlled the frequency of firing the pistons was created. This way the user would not have to calculate the trigger speeds necessary to attain different motor speeds. As can be seen from the code in Figure 35 this is the previous program with different calculations to determine the delays. The frequency specified is the number of pistons fired per second. The conversion for this to delay between piston fires is given as:

$$Delay = 1000/Frequency$$

This is rounded to the nearest integer, which means that input frequency is only approximate, not exact.

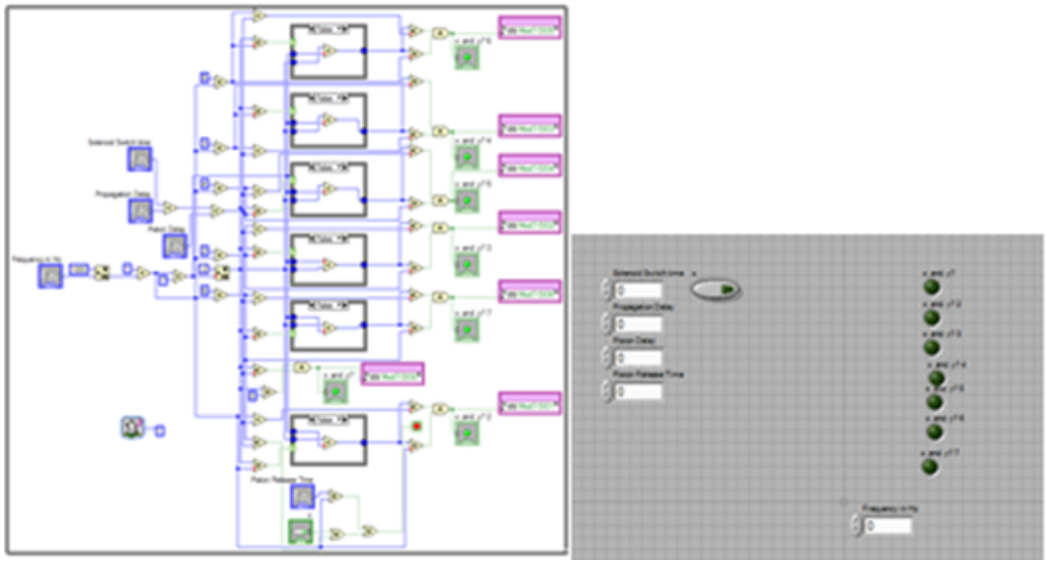

Figure 35: Motor Frequency Control GUI and Motor Frequency Control Block Diagram

The code being run is similar to the first program, except the delays are calculated by the program based on experimental results instead of being input by the user. Unfortunately some of the assumptions that were made when designing this program turned out to be incorrect. The GUI shows fields for Solenoid Switch Time, Propagation Delay, Piston Delay, and Piston Release time. These are intended to prevent the program from making a loop that will jam the motor. However some initial tests with the motor showed that the propagation delay determined from earlier tests was not the effective delay when running the motor. The difference is due to the fact that the delay of a completely unpressurized air line was tested for determining the timing relationships. However when running the motor, the time between a single valve being turned on twice is not great enough for the line to completely depressurize. This means that when the valve was turned on again it took less time for the line to fully pressurize than it did in the tests. To determine the *effective* propagation delay a test was run with the pressure sensor hooked into a line going to the motor and these results were used in subsequent control programs.

Developing Software to Test Motor Performance

The speed test was to verify that the motor shaft was rotating at a speed equivalent to its predicted speed based on the frequency of the pistons. For the first run of this test, only a potentiometer was used to check the speed. While a shaft encoder would have had higher accuracy, less noise, and would have allowed for easier interpretation of data, we did not have access to one in time to run the tests. Instead the potentiometer was used. This was an infinite turn potentiometer which gave a voltage proportional to the degree of rotation, resetting at a certain position to 0v. This signal was read

in the same manner as the pressure sensor, by being hooked into the cRIO Analog Input. Since the input was so similar, the differences in this controller from the propagation testing one was almost entirely in the output signal and the sampling rate. Because there were seven solenoids that had to be run instead of one, a different control loop was created. It is almost identical to the one used in GUI for running the motor. The sole difference is that instead of controlling each solenoid independently, there is one set of timing values used for all seven solenoids. The end result was a program that could run the motor while simultaneously polling an Analog input, Figure 36.

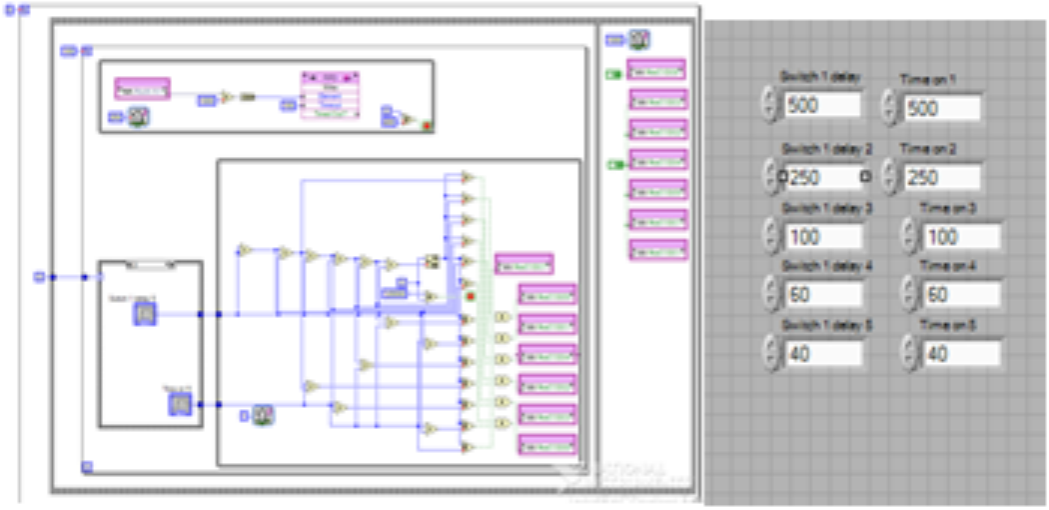

Figure 36: Speed Testing GUI and Speed Testing Block Diagram

The speed testing cRIO code is essentially two preexisting programs put together. The motor is run with essentially the same code as GUI for Running Motor. The only difference is that instead of controlling each solenoid independently, all of them have the same delay values. Also the user can enter up to five values to test, each one that will run 100 two minute tests. The second part is the same polling code from the propagation testing, just with a different sensor hooked into the analog input. The last part of the code turns off all of the solenoids, see Figure 37.

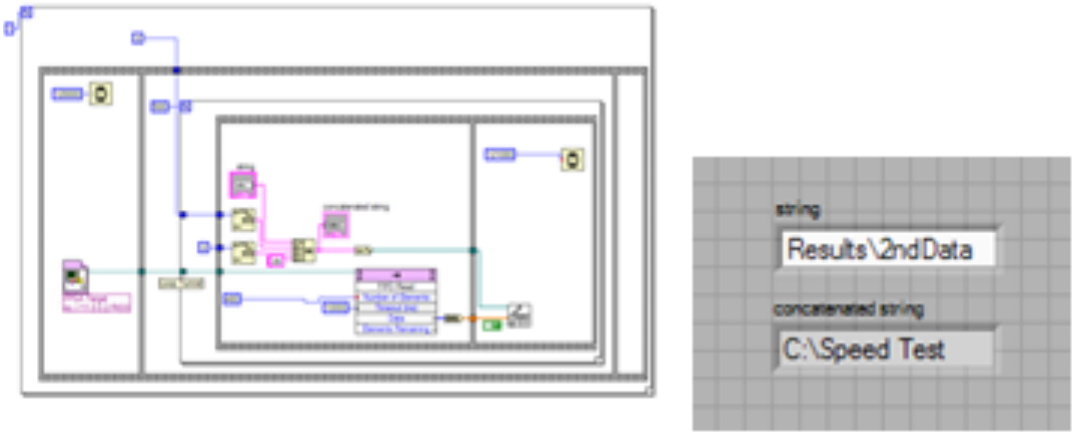

Figure 37: Run Speed Test GUI and Run Speed Test Block Diagram

The host code is identical to the host code for propagation testing, except with some variables changed and a different program being run.

The motor propagation delay testing code is similar to the code above. The loop to run the motors is identical, but the loop is run for less time, and the sampling of the Analog Input is done at a much faster rate. To get a clear pattern for propagation delay it is necessary to have more data points in the same period of time than for speed. The pressure sensor is hooked to one piston, and there is a window of only 40-500ms where it is being turned on, so it is necessary to get as much information as possible during this time. The reason the loop runs for less time is related to the sampling rate. The method of data transfer, FIFO, is useful in many respects but it is limited on how many data points can be held in the buffer at a time. The upper limit is determined by the available memory in the cRIO, and 4,096 data points of I64 data type was as much as it could handle. As such, the propagation data could only be collected for 4,096 data points before reaching the limit. Since the sampling rate is 2 ms, this is only 8 seconds worth of data. This ends up being roughly 11-25 cycles of pressurizing depending on the frequency the pistons are being run.

Results

Propagation Delay Testing

The goal of the propagation delay testing is to determine the delay from when the solenoid opens to when full pressure has been applied to the pressure sensor. In this experiment the full pressure is 80 psi. In the following sections the propagation delay test results will be split up by the two diameters and the direct connection testing conditions. When analyzing the data for the propagation tests, 10-20 percent of the tests had results that were vastly different from the rest. These results were removed from the following data analysis.

Direct Connection

The resulting median value and standard deviation are shown in Table 3.

Mean	Standard Deviation
21.6	2.0

Table 3: Direct Connection Median Value

Figure 38 contains the graph showing the average values of the direct connection tests.

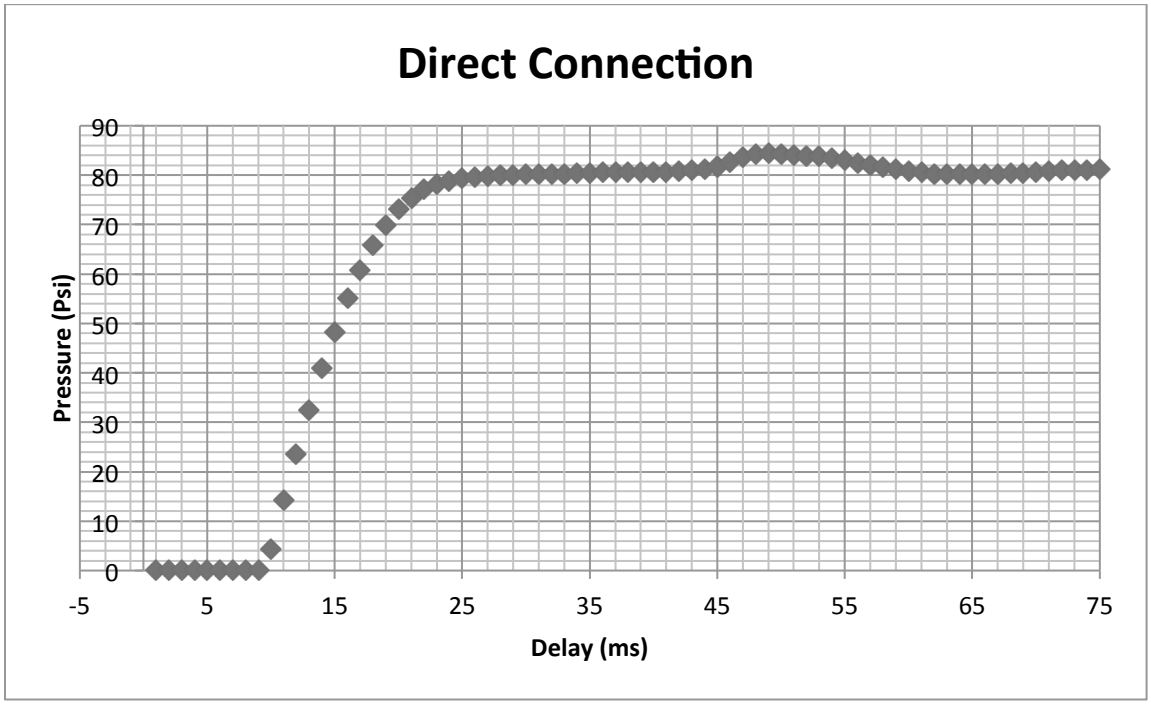

Figure 38: Plot of Average Sensor Value vs. Time, Direct Connection

The graph shows the behavior, where the pressure doesn't change at all for the first 10ms, then steadily rises to full pressure at 21ms, for a rise time of 11ms.

Diameter of 1/4"

The resulting median value, standard deviation, and graphs for each length at the 1/4" diameter can be found in this section.

Mean	Standard Deviation
134	1100.6

Table 4: Diameter 1/4", Length 5'

Table 4 above shows the mean and standard deviation of the 1/4" by 5' pneumatic tubing.

Mean	Standard Deviation
360.1	47.9

Table 5: Diameter 1/4", Length 10'

Table 5 above shows the mean and standard deviation of the 1/4" by 10' pneumatic tubing.

Mean	Standard Deviation
351.8	7.3

Table 6: Diameter 1/4", Length 15'

Table 6 above shows the mean and standard deviation of the 1/4" by 15' pneumatic tubing

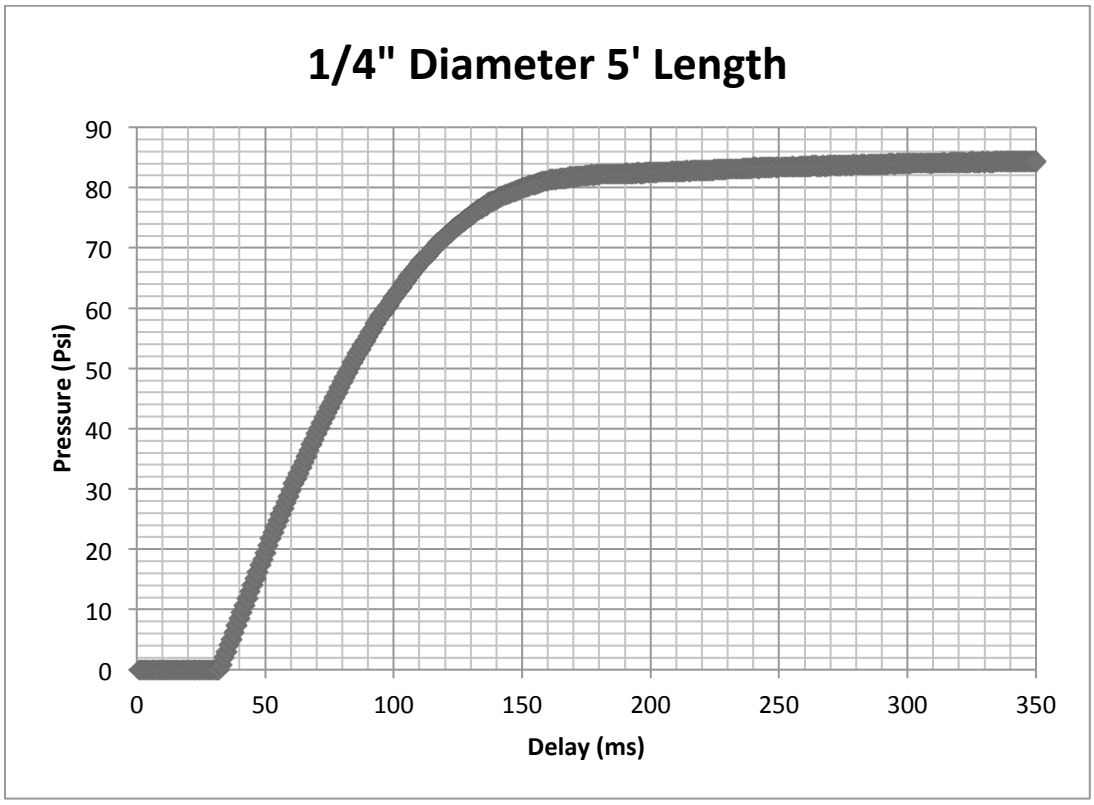

Figure 39: Plot of Sensor Value vs. Time, 1/4" Diameter: 5' Length

Figure 39 shows the data of sensor value as a function of time for all the tests of the 1/4" diameter, 5' length connections.

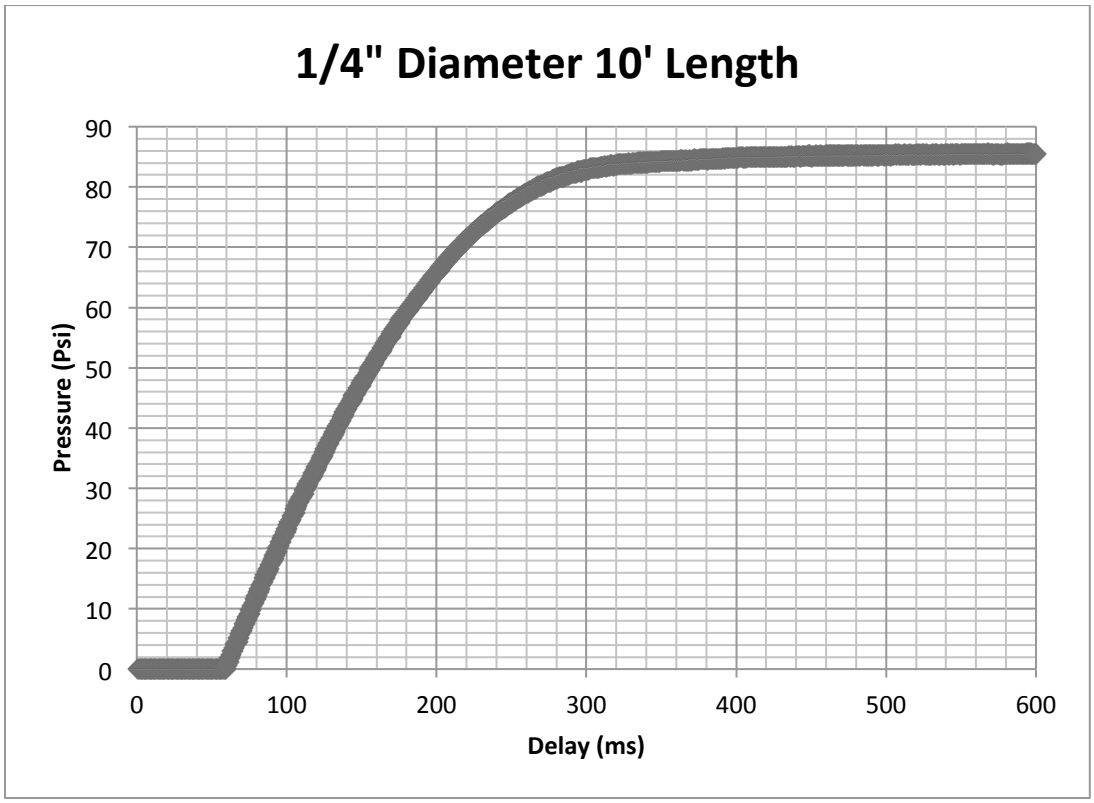

Figure 40: Plot of Sensor Value vs. Time, 1/4" Diameter: 10' Length

Figure 40 shows the data of sensor value as a function of time for all the tests of the 1/4" diameter, 5' length connections.

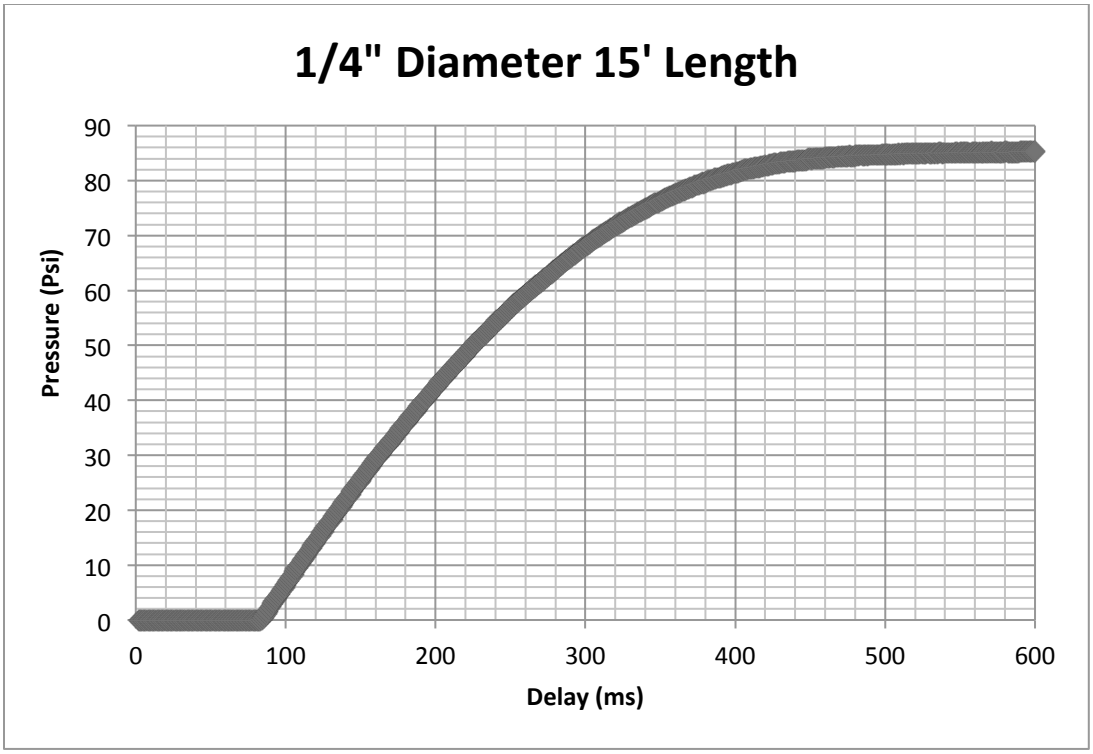

Figure 41: Plot of Sensor Value vs. Time, 1/4" Diameter: 15' Length

Figure 41 shows the data of sensor value as a function of time for all the tests of the 1/4" diameter, 5' length connections.

Diameter of 5/32"

The resulting median value, standard deviation, and graphs for each length at the 5/32" diameter can be found in this section.

Mean	Standard Deviation
71.1	1.25

Table 7: Diameter 5/32", Length 5'

Table 7 above shows the mean and standard deviation of the 5/32" by 5' pneumatic tubing.

Mean	Standard Deviation
121.5	9.09

Table 8: Diameter 5/32", Length 10'

Table 8 above shows the mean and standard deviation of the 5/32" by 10' pneumatic tubing.

Mean	Standard Deviation
176.4	3.99

Table 9: Diameter 5/32", Length 15'

Table 9 above shows the mean and standard deviation of the 5/32" by 15’ pneumatic tubing.

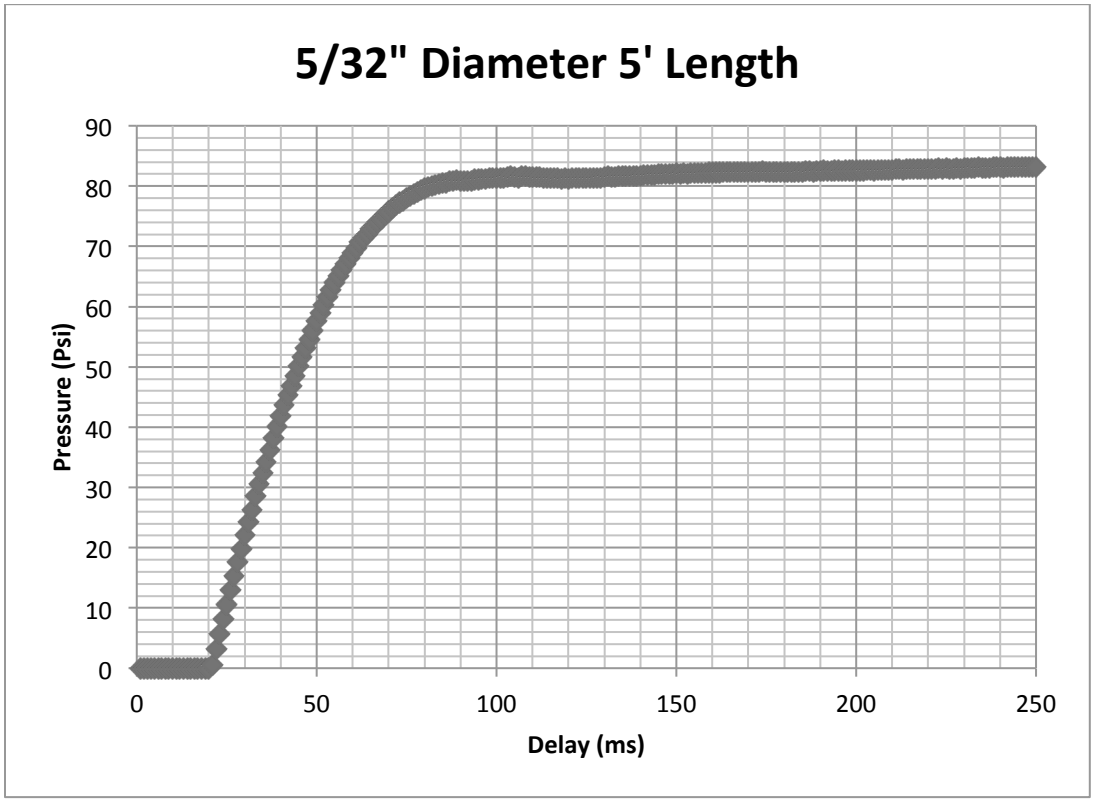

Figure 42: Plot of Sensor Value vs. Time, 5/32" Diameter: 5' Length

Figure 42 above shows the data of sensor value as a function of time for all the tests of the 5/32” diameter, 5’ length connections.

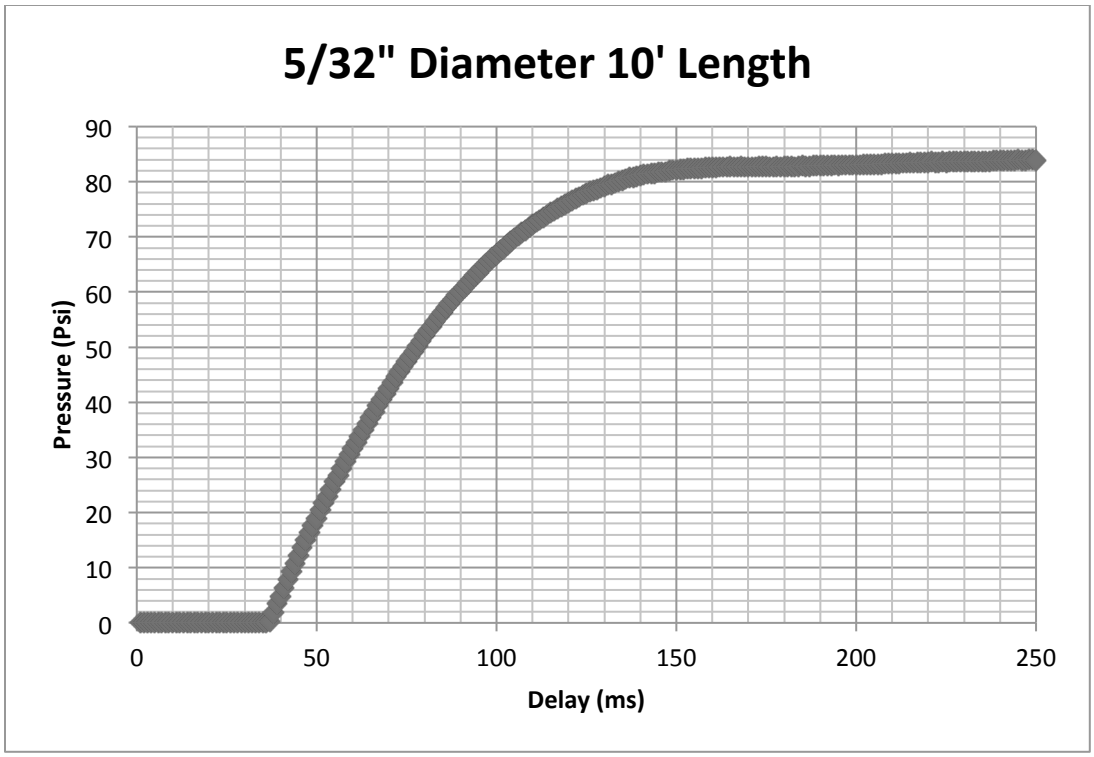

Figure 43: Plot of Sensor Value vs. Time, 5/32" Diameter: 10' Length

Figure 43 shows the data of sensor value as a function of time for all the tests of the 5/32" diameter, 10' length connections.

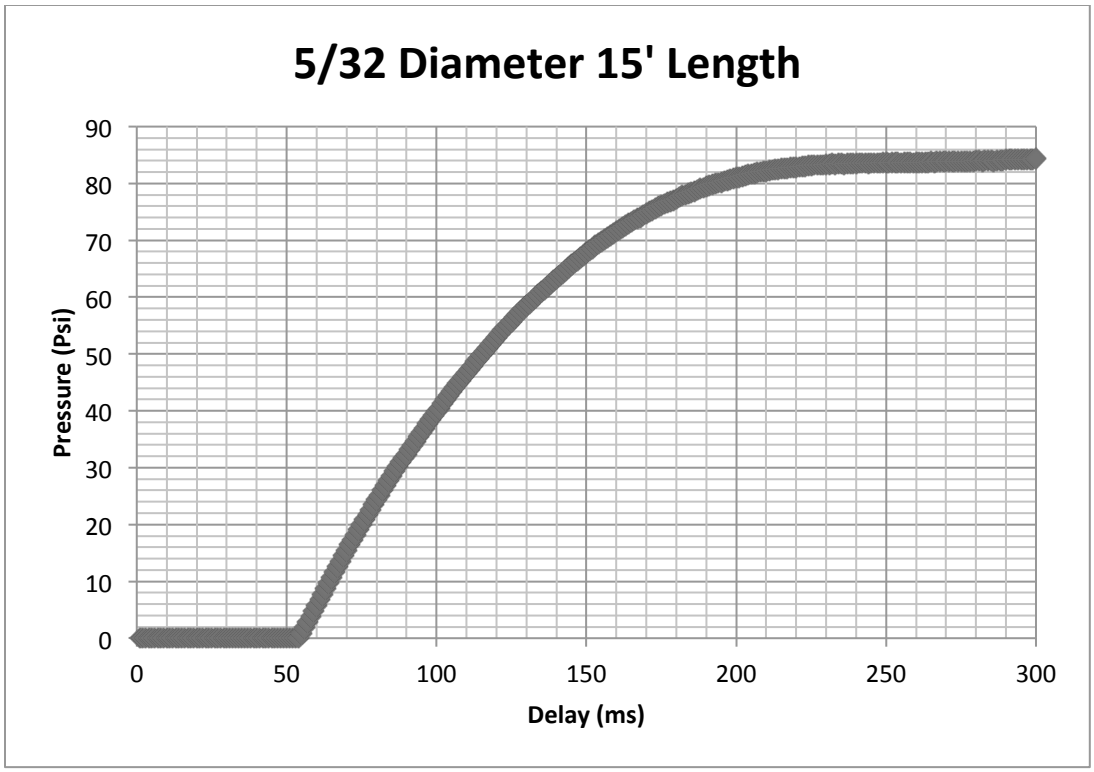

Figure 44: Plot of Sensor Value vs. Time, 5/32" Diameter: 15' Length

Figure 44 shows the data of sensor value as a function of time for all the tests of the 5/32" diameter, 15' length connection.

Graph Showing All Tests

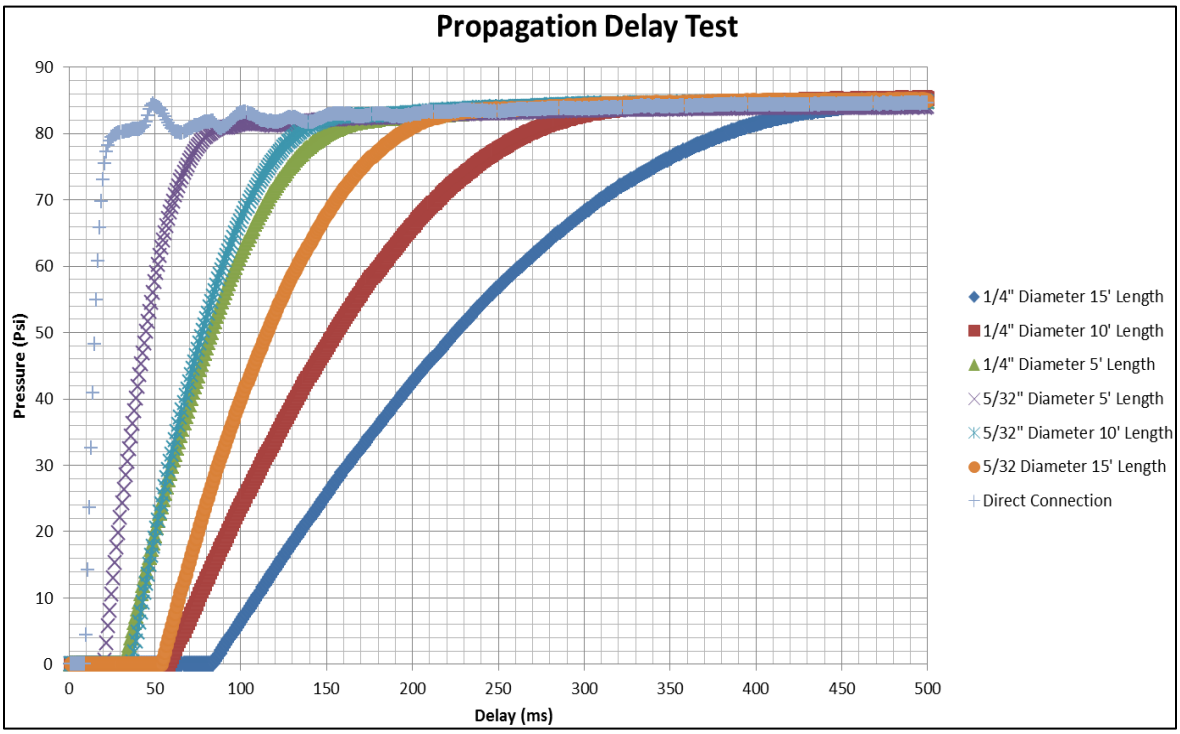

Figure 45: Graph for all Propagation Tests

Figure 45 is a graph representing all of the propagation testing results for the direct connection, 1/4" diameter, and 5/32” diameter

Speed Testing

The goal of the Speed Testing was to determine the speed of the actuator and its overall consistency. The sections below are the results for the speed testing split up into sections differentiated by the frequency at which the actuator was operated. When analyzing the data for the speed tests, 10-20 percent of the tests had results were corrupted. These results were removed from the following data analysis.

500ms Test

Figure 46 shows the total degrees traveled by each of the 500ms tests.

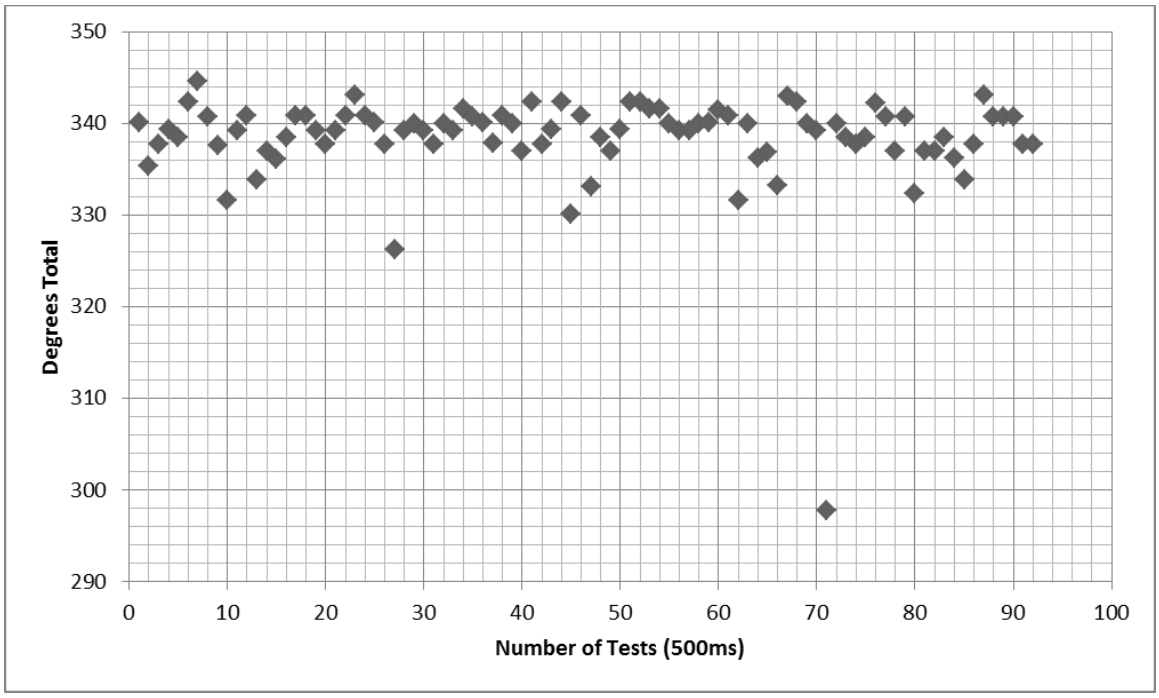

Figure 46: Total degrees traveled for each test (500ms)

Table 10 shows the percent error between the expected degrees traveled and the actual degrees traveled.

Expected Degrees	Actual Degrees (Average)	Percent Error
342.9	338.4	1.30

Table 10: Consistency at 500ms

The resulting mean speed and standard deviation for the 500ms test run data can be seen in Table 11.

Mean (Velocity)	Standard Deviation
2.82	0.044

Table 11: Velocity at 500ms

Figure 47 below shows the angular velocity at 500ms for each of the tests.

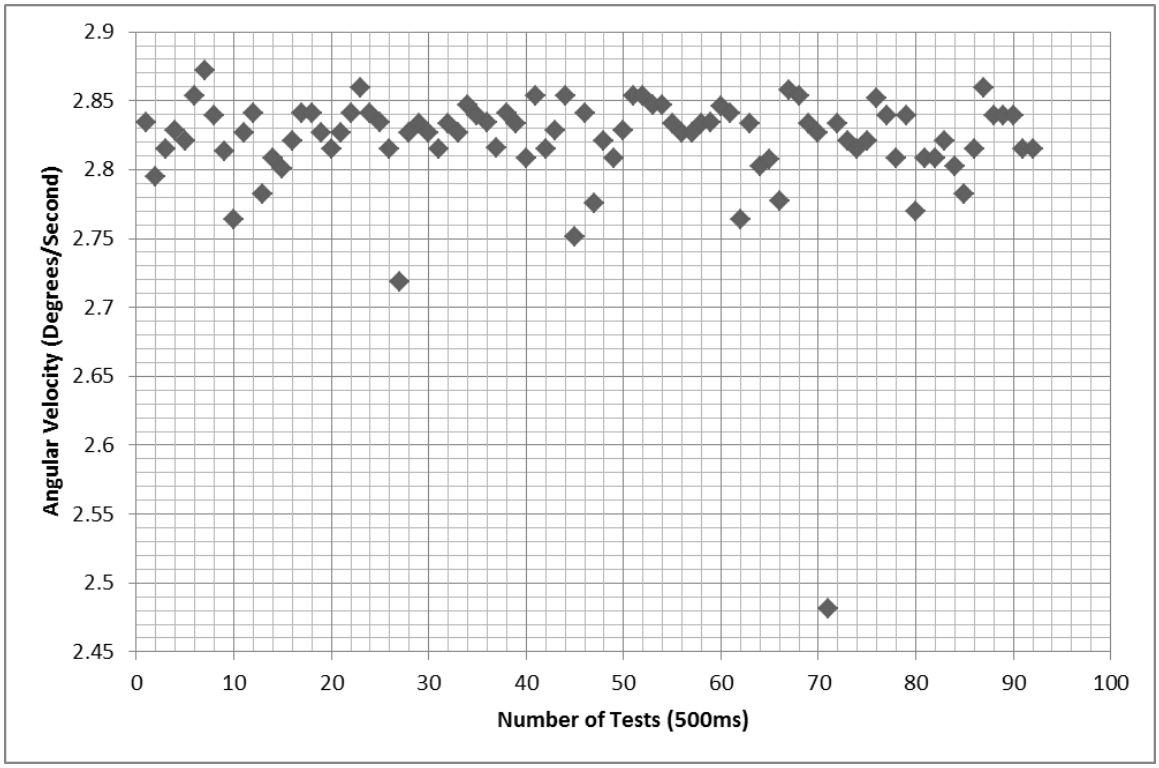

Figure 47: Velocity values for each test (500ms)

250ms Test

Figure 48 below shows the total degrees traveled by each of the 250ms tests.

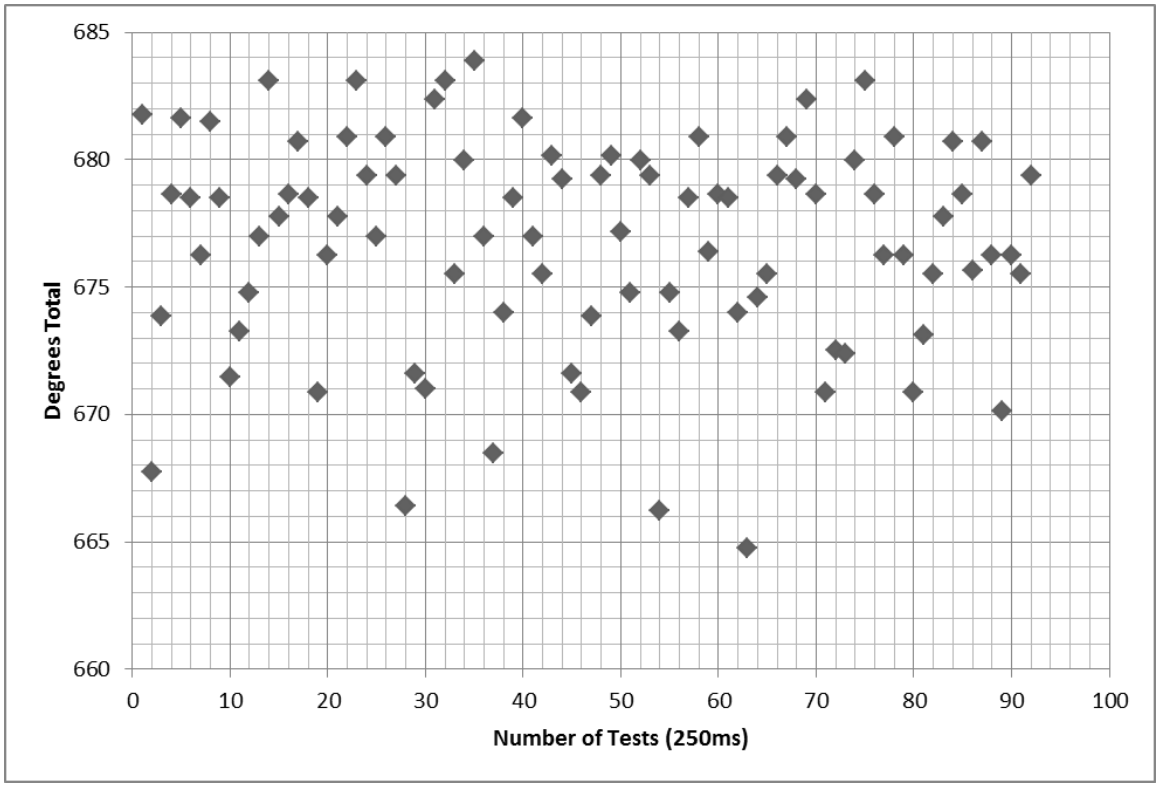

Figure 48: Total Degrees traveled for each test (250ms)

Table 12 shows the percent error between the expected degrees traveled and the actual degrees traveled.

Expected Degrees	Actual Degrees (Average)	Percent Error
685.7	676.8	1.29

Table 12: Consistency at 250ms

The resulting mean speed and standard deviation for the 250ms test run data can be seen in Table 13.

Mean (Velocity)	Standard Deviation
5.64	0.035

Table 13: Velocity at 250ms

Figure 49 shows the angular velocity at 250ms for each of the tests.

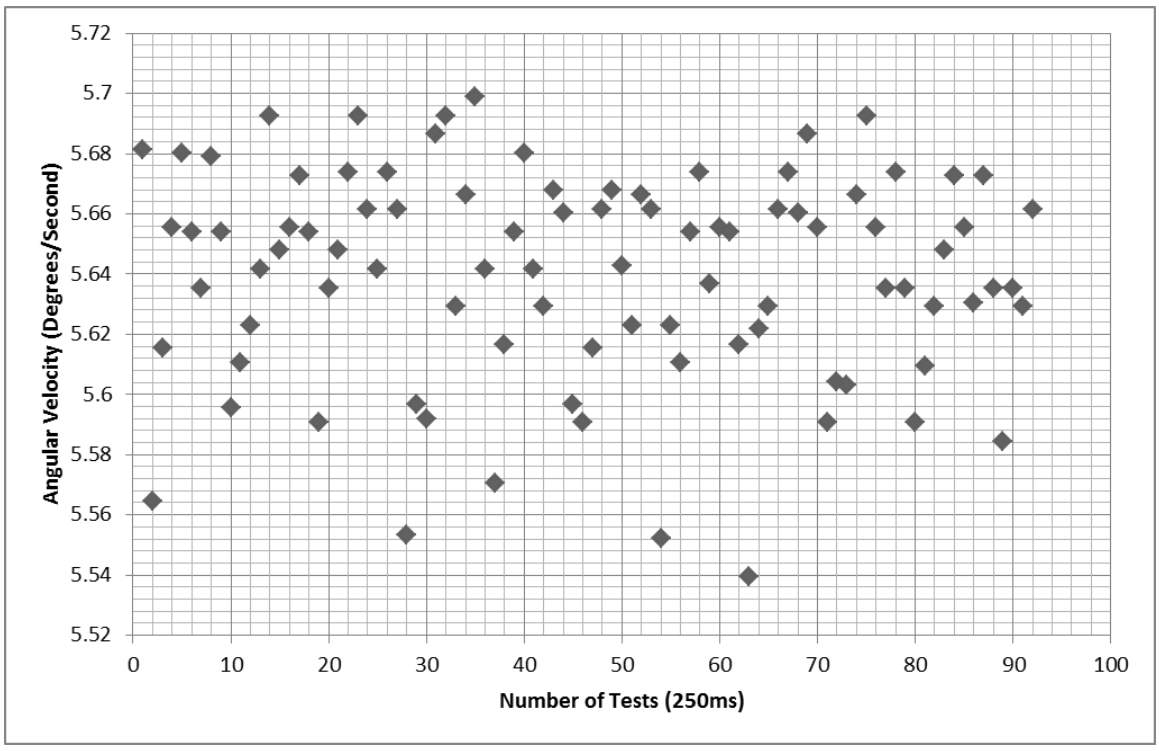

Figure 49: Velocity values for each test (250ms)

100ms Test

Figure 50 shows the total degrees traveled by each of the 100ms tests.

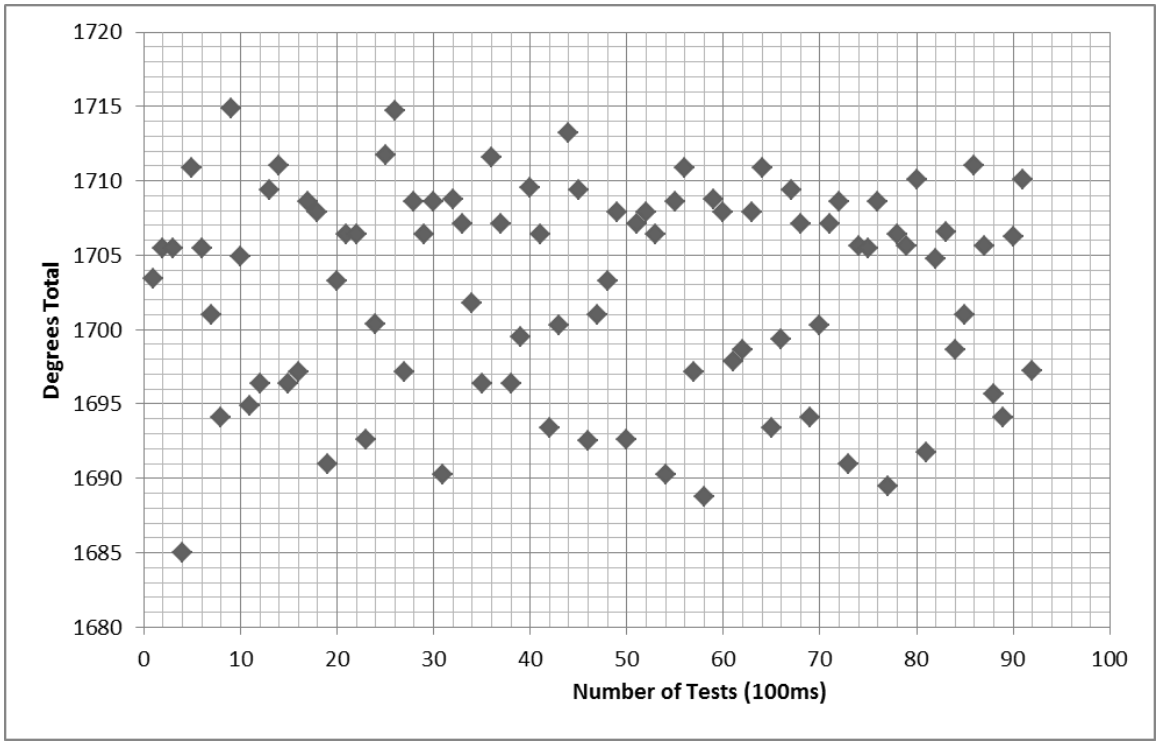

Figure 50: Total degrees traveled for each test (100ms)

Table 14 shows the percent error between the expected degrees traveled and the actual degrees traveled.

Expected Degrees	Actual Degrees (Average)	Percent Error
1714.3	1702.8	0.67

Table 14: Consistency at 100ms

The resulting mean speed and standard deviation for the 100ms test run data can be seen in Table 15.

Mean (Velocity)	Standard Deviation
14.19	0.058

Table 15: Velocity at 100ms

Figure 51 shows the angular velocity at 100ms for each of the tests.

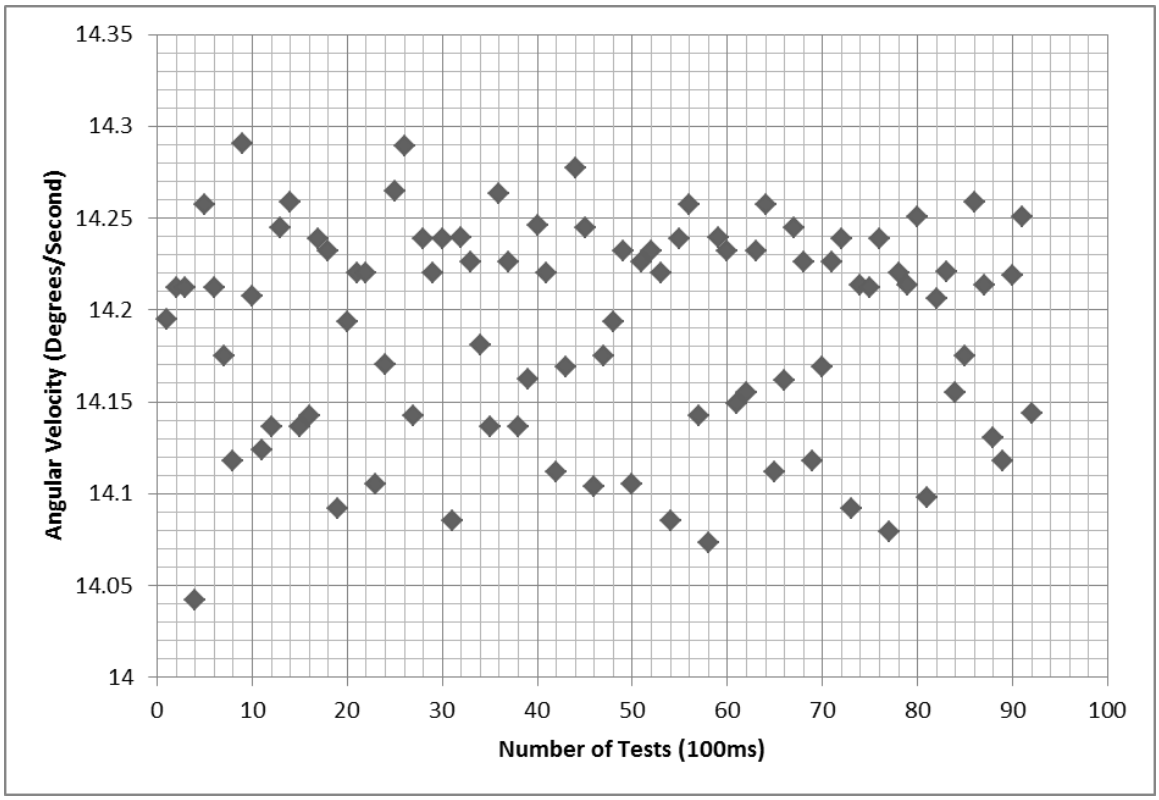

Figure 51: Velocity for each of the tests (100ms)

60ms Test

Figure 52 shows the total degrees traveled by each of the 60ms tests.

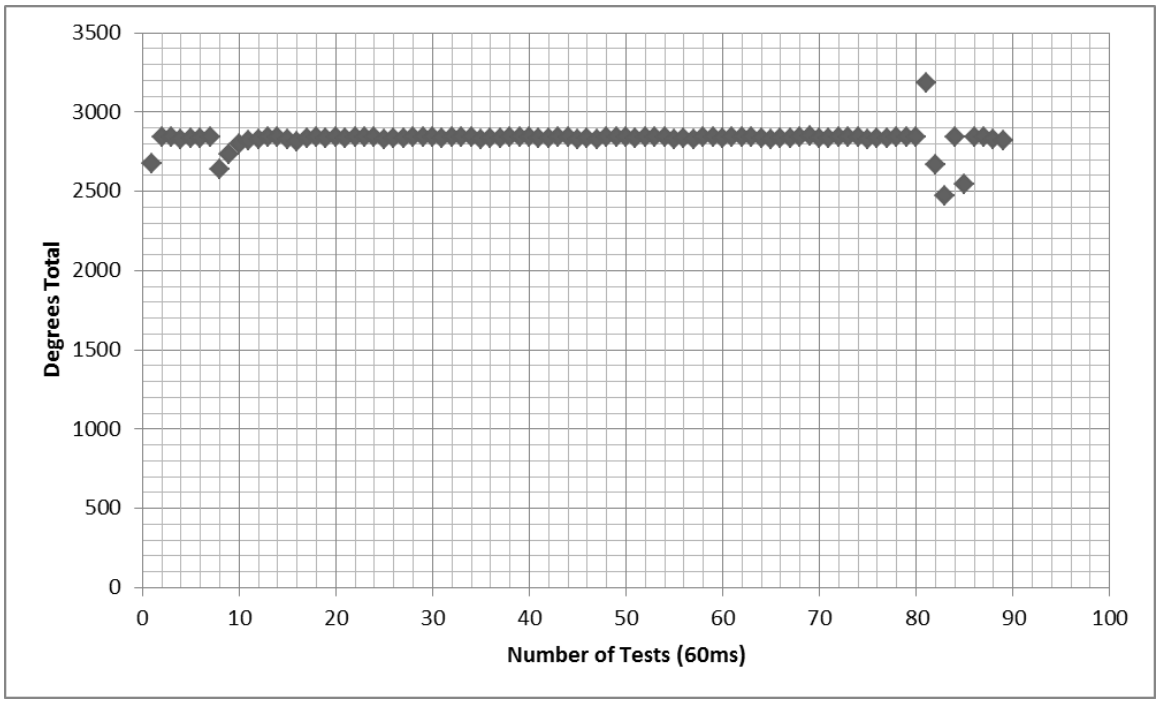

Figure 52: Total Degrees traveled for each test (60ms)

Table 16 shows the percent error between the expected degrees traveled and the actual degrees traveled.

Expected Degrees	Actual Degrees (Average)	Percent Error
2857.1	2789.7	2.36

Table 16: Consistency at 60ms

The resulting mean speed and standard deviation for the 60ms test run data can be seen in Table 17.

Mean (Velocity)	Standard Deviation
23.6	0.587

Table 17: Velocity value (60ms)

Figure 53 shows the angular velocity at 60ms for each of the tests.

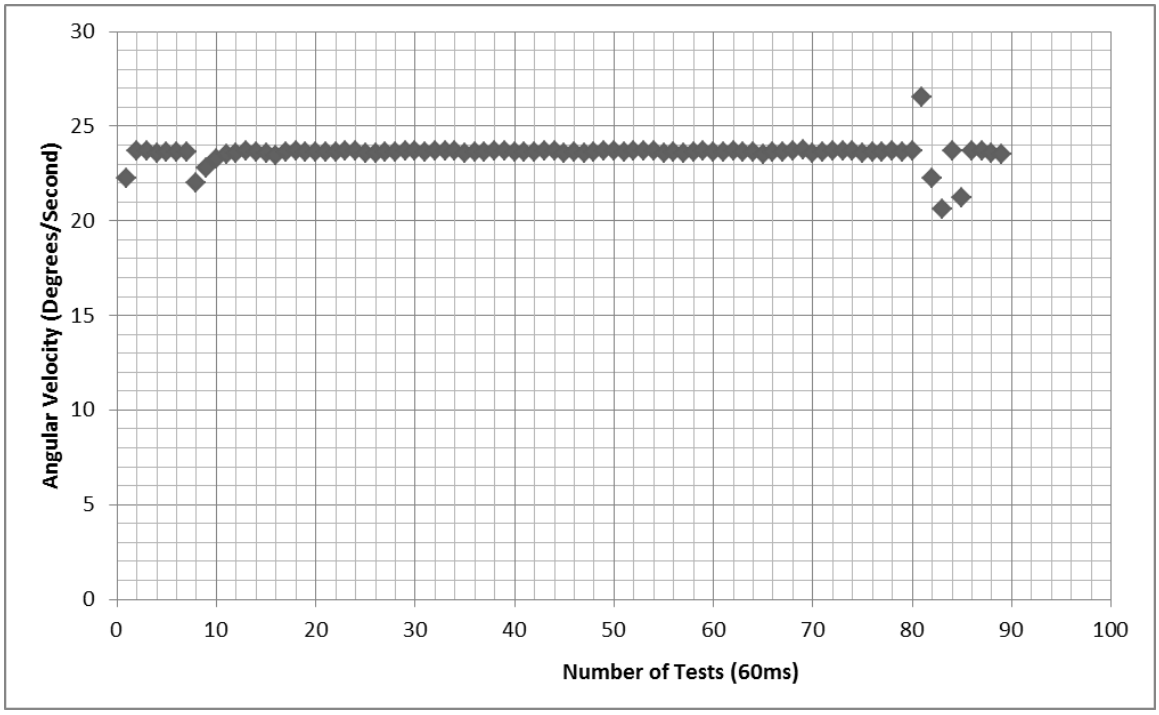

Figure 53: Velocity Values for each test

40ms Test

Figure **54** shows the total degrees traveled by each of the 40ms tests. This graph shows significant error in the test. For this reason none of the other analysis were performed for this test.

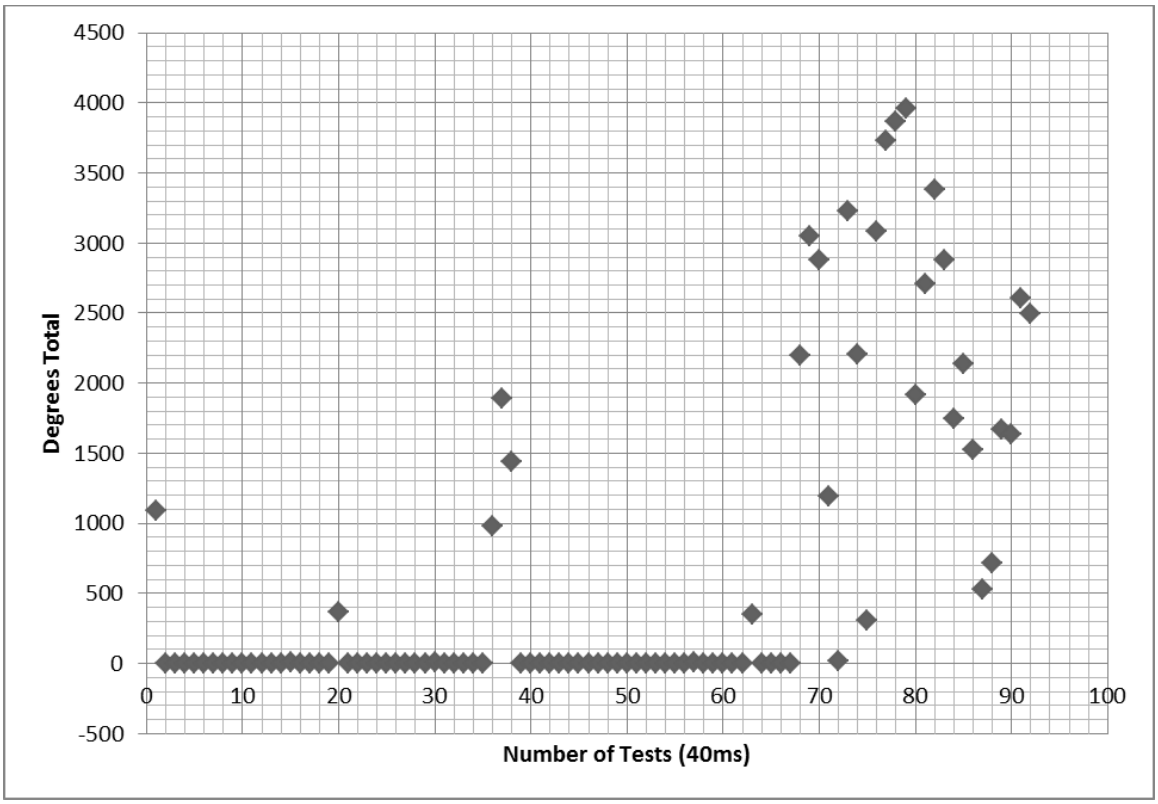

Figure 54 - Total degrees traveled for each test (40ms)

100 Revolution Tests

In addition to the two minute tests, a test was done that had the motor perform 100 revolutions at specific time intervals, and then observe the actual number of revolutions. The number of revolutions was recorded by measuring the beginning and ending position of the potentiometer, calculating the difference, then adding that value to the number of revolutions counted by the VI running the test. Two different time intervals were tested in this manner, 200 and 300ms.

200msTest

The 200ms test yielded an over-rotation of 2.0 degrees after 100 revolutions. This was a percent error of .005%, which is small enough to be indistinguishable from noise in the measurement.

300ms Test

The 300ms test yielded an over-rotation of 3.6 degrees after 100 revolutions. This was a percent error of .01%, which is small enough to be indistinguishable from noise in the measurement.

Torque Testing

The results of the torque section can be seen in Table 18. From the table the maximum weight that the PRiSM could lift at 60 psi was 700 grams. This resulted in an output torque of 436 N*mm. An additional test was conducted with the pressure increased to 80 psi. This test resulted in the PRiSM lifting 1200 grams with an output torque of 747 N*mm.

Pressure (psi)	Maximum Weight (g)	Torque Output (Nmm)
60	700	436
80	1200	747

Table 18: Torque Test Results

Discussion

Propagation Delay Testing

Overall the propagation delay testing went very well. The cRIO proved it was a worthy candidate to perform this test as well as future actuator tests. More propagation tests using the cRIO could have led to more results but the data from one hundred tests seemed fairly conclusive. On several runs for each test though there were significantly higher propagation delays. Some were even delayed the entire four seconds; so it never reached 80 psi. These results were in random intervals but normally appeared in the later tests. After evaluating and considering the age of the valves used that these were due to the solenoid sticking closed when pulled high. For the ones that never reached 80 psi the solenoid stuck throughout the whole test and for those that took significantly longer the valve stuck for a portion of the time.

When the results of bad delays were ignored the results were much more consistent. The direct connection between the solenoid and pressure sensor yielded a delay of 21ms. This delay is the time it took the valve to fully open and let full pressure into the system. So for each solenoid picked to operate it can be accepted that a 21ms delay will occur.

The 1/4” tubing had the highest delays overall. The lowest delay value was 134ms with the 5’ length of tubing. The 10’ had a delay value of 390ms while the 15’s section only had a 352.5ms delay value. This result raises eyebrows until the curves are taking into consideration. For the 10’ section the curve of values had a slope much higher than the 15’ section. When looking at the numbers though, the 10’ section had more valve problems as discussed earlier resulting in more erratic numbers. From these numbers the only logical choice would be the 5’ section of 1/4” tubing based on its lower delay value.

The 5/32” tubing gave the lowest and most desired delays. The lowest valve for the 5/32” tubing was the 5’ section with a delay of only 71ms. The 10’ section had a 121ms delay and the 15’ section had a 176ms delay. These values were very consistent and showed a roughly 50ms delay for each 5’ of additional tubing.

The final choice for the actuator design after reviewing all the options was the 10’ length of the 5/32” diameter tubing. This tubing had a delay of only 121ms which is fast enough to get multiple cycles per second. The tubing is smaller and much easier to manipulate than the 1/4" tubing. Being smaller in diameter means it takes up less space and if multiple actuators are going to be used, the more space

saved in tubing without the sacrifice in performance is crucial. The length of 10' was chosen to keep ferrous materials out of the MRI environment. This ferrous material would be the solenoids and the processing unit to control them.

Speed Testing

The initial speed tests that were run showed errors large enough to reach the conclusion that the motor was not able to be run open loop. However the data that was collected showed that the error might have been with the test design instead of the motor's performance. The data would sometimes show implausible results such as certain tests having gone much farther than they should have, and a large number of unusable test results. To iron out these issues a new data collection method was devised. This method used the cRIO to calculate the number of revolutions on its own, to avoid any errors propagating from data transfer. The new test was also ran for a much longer time period, 1.5-2 hours instead of two minutes.

The results of this test show a drastically smaller percent error, from values of 2-3% to .01%. With the errors measured in the second test, the motor could be run open loop with negligible error. This is an important result because it allows for much simpler control of the motor's actuation.

Torque Testing

The results of the torque testing were successful in identifying the maximum output torque at which the PRiSM could still be operational. At 60psi the torque was 436 N*mm which is around 130 N*mm greater than the PneuStep's maximum output torque at the same pressure. When the pressure was increased to 80psi the PRiSM outputted an increased torque of 747 N*mm this was around 300 N*mm greater than the maximum torque for the PneuStep at that same pressure.

The PRiSM has improved upon the current torque performance benchmark in pneumatic actuator technologies. Further improvements and revisions to the motor such as changing the material to decrease internal friction and changing the pitch of the gear tooth could improve the maximum torque. Since the motor is dependent on timed pulses of air actuating a piston, the motor torque can be improved by making sure that the next piston in the series is actuated in sequence with the release of previous piston. Even though improvements can be made the test was a success and shows the PRiSM can be used for applications where more torque is a requirement.

Bibliography

AIM Lab. (n.d.). *Automation and Interventional Medicine*. Retrieved November 29, 2011, from Worcester Polytechnic Institute: http://aimlab.wpi.edu/

Cutting, C., Taylor, R., Bockstein, R., Khorramabadi, D., Haddad, B., Kalvin, A., et al. (n.d.). Computer aided planning and execution of cranofacial surgical procedures. *Proceeding of IEEE Engineering in Medicine and Biology Conference.*

Fischer, G. S., Iordachita, I., Csoma, C., Tokuda, J., DiMaio, S. P., Tempany, C., et al. (2008). Mri-Compatible Pneumatic Robot for Tranperineal Prostate Needle Placement. *IEEE/ASME Transactions on Mechatronics*, 295-305.

Fischer, G. S., Krieger, A., Iordachita, I., Csorra, C., Whitcomb, L., & Fichtinger, G. (2008). MRI Compatibility of Robot Acutation Techniques - A Comparative Study. *11th International Conference on Medical Image Computing and Computer-Assisted Intervention*, (pp. 509-517). New York.

Gassert, R., Burdet, E., & Chinzei, K. (2008). Opportunities and Challenges in MR-Compatible Robotics. *Engineering in Medicine and Biology Magazine*, 15-22.

Hata, N., Morrison, P. R., Kettenbach, J., Black, P., Kikinis, R., & Jolesz, F. A. (1998). Computer-Assisted Intra-Operative Magnetic Resonance Imaging Monitoring of Interstitial Laser Therapy in the Brain. *J. Biomed*, 304.

Hong, J., Hata, N., Konishi, K., & Hashizume, M. (2008). Real-time magnetic resonance imaging driven by electromagnetic locator for interventional procedure and edoscopic therapy. *Surg Endosc*, 552-556.

Johns Hopkins Medicine. (2005). *URobotics: Urology Robotics*. Retrieved November 29, 2011, from Johns Hopkins Medicine: http://urobotics.urology.jhu.edu/projects/PneuStep/

Lee Spring. (2011). *Technical Specifications and Engineers Notes*. Retrieved November 29, 2011, from Lee Spring: http://www.leespring.com/tolerance1.asp

Mallot, J. (1997). *Hazards of Ferrous Material in MRI: a case report.* Radiol Technology.

McMaster-Carr. (n.d.). *End Mills, Part Number 3073A62*. Retrieved September 21, 2011, from McMaster-Carr: http://www.mcmaster.com/#3073a62/=f8m0t0

Nanomotion. (n.d.). *How It Works*. Retrieved November 29, 2011, from Nanomotion: A Johnson Electric Company: http://www.nanomotion.com/

Narayanan, R., Kurhanewicz, I., Shinohara, K., Crawford, D., Bargawi, A., Simoneau, A., et al. (n.d.). MRI/TRUS Fusion for Prostate Biopsy: Early Results and Clinical Feasibility. *Proceedings 17th Scientific Meeting, International Society for Magnetic Resonance in Medicine*, (p. 2247).

Plastics Unlimited Inc. (2011). *About Us*. Retrieved November 29, 2011, from Plastics Unlimited Inc.: http://www.plasticsunlimitedinc.com/

Random House Dictionary. (2011). Retrieved November 29, 2011, from Dictionary.com: http://dictionary.reference.com/browse/phase

Staff, D. W. (2008, October 20). *Pneumatic Step Motor is First Fully MRI-compatible Motor.* Retrieved December 5, 2011, from Design Worls: http://www.designworldonline.com/articles/2813/267/Pneumatic-Step-Motor-is-First-Fully-MRI-compatible-Motor.aspx

Su, H., Zervas, M., Cole, G. A., Furlong, C., & Fischer, G. S. (2011). Real-time MRI-Guided Needle Placement Robot with Integrate Fiber Optic Force Sensing. *IEEE ICRA 2011 International Conference on Robotics and Automation*, (pp. 1583-1588). Shanghai.

Taylor, R. e. (1996). An Overview of Computer-Integrated Surgery at the IBM Thomas J. Watson Research Center. *IBM Journal of Research and Development*, 163.

Tokuda, J., Tuncali, K., Iordachita, I., Song, S. E., Fedorov, A., Oguro, S., et al. (n.d.). Preliminary Accuracy Evaluation of 3T MRI-Guided Transperineal Prostate Biopsy with Grid Template. *ISMRM*.

Tse, Z. T., Chan, Y., Janssen, H., Hamed, A., Young, I., & Lamperth, M. (n.d.). Piezoelectric actuator design for MRI elastography implementation and vibration issues. *The International Journal of Medical Robotics and Computer Assisted Surgery, 7*, 353-360.

Universal Laser Systems. (2011). *VLS 4.6*. Retrieved November 29, 2011, from Universal Laser Systems: http://www.ulsinc.com/products/vls460/

Wang, Y., Cole, G. A., Su, H., Pilitis, J. G., & Fischer, G. S. (2009). Mri Compatibility Evaluation of a Piezoelectric Actuator System for a Neural Interventional Robot. *31st Annual International Conference of the IEEE Engineering in Medicine and Biology Society.* Minneapolis.

Zuo, S., Yamanaka, N., Sato, I., Masamune, K., Liao, H., Matsumiya, K., et al. (2008). MRI-Compatible Rigid and Flexible Outer Sheath Device with Pneumatic Locking Mechanism for Minimally Invasive Surgery. *Proc. MIAR*, (pp. 210-219).

Appendix A – Experimental Data

See CD.

Appendix B – LM134 Performance Characteristics

Typical Performance Characteristics (Continued)

Turn-On Voltage

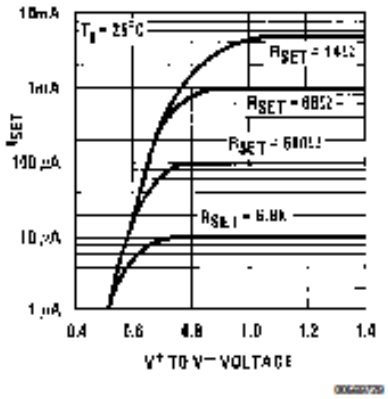

Ratio of I_{SET} to I_{BIAS}

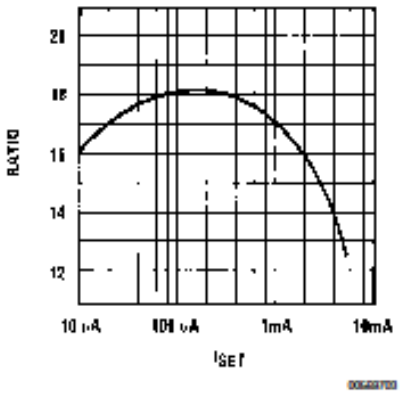

Application Hints

The LM134 has been designed for ease of application, but a general discussion of design features is presented here to familiarize the designer with device characteristics which may not be immediately obvious. These include the effects of slewing, power dissipation, capacitance, noise, and contact resistance.

CALCULATING R_{SET}

The total current through the LM134 (I_{SET}) is the sum of the current going through the SET resistor (I_R) and the LM134's bias current (I_{BIAS}), as shown in *Figure 1*.

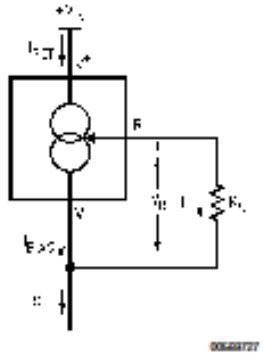

FIGURE 1. Basic Current Source

A graph showing the ratio of these two currents is supplied under **Ratio of I_{SET} to I_{BIAS}** in the Typical Performance Characteristics section. The current flowing through R_{SET} is determined by V_R, which is approximately 214µV/°K (64 mV/298°K ~ 214µV/°K).

$$I_{SET} = I_R + I_{BIAS} = \frac{V_R}{R_{SET}} + I_{BIAS}$$

Since (for a given set current) I_{BIAS} is simply a percentage of I_{SET}, the equation can be rewritten

$$I_{SET} = \left(\frac{V_R}{R_{SET}}\right)\left(\frac{n}{n-1}\right)$$

where n is the ratio of I_{SET} to I_{BIAS} as specified in the Electrical Characteristics Section and shown in the graph. Since n is typically 18 for 2µA ≤ I_{SET} ≤ 1mA, the equation can be further simplified to

$$I_{SET} = \left(\frac{V_R}{R_{SET}}\right)(1.056) = \frac{227\ \mu V/°K}{R_{SET}}$$

for most set currents.

SLEW RATE

At slew rates above a given threshold (see curve), the LM134 may exhibit non-linear current shifts. The slewing rate at which this occurs is directly proportional to I_{SET}. At I_{SET} = 10µA, maximum dV/dt is 0.01V/µs; at I_{SET} = 1mA, the limit is 1V/µs. Slew rates above the limit do not harm the LM134, or cause large currents to flow.

THERMAL EFFECTS

Internal heating can have a significant effect on current regulation for I_{SET} greater than 100µA. For example, each 1V increase across the LM134 at I_{SET} = 1 mA will increase junction temperature by ~0.4°C in still air. Output current (I_{SET}) has a temperature coefficient of ~0.33%/°C, so the change in current due to temperature rise will be (0.4)(0.33) = 0.132%. This is a 10:1 degradation in regulation compared to true electrical effects. Thermal effects, therefore, must be taken into account when DC regulation is critical and I_{SET} exceeds 100µA. Heat sinking of the TO-46 package or the TO-92 leads can reduce this effect by more than 3:1.

SHUNT CAPACITANCE

In certain applications, the 15 pF shunt capacitance of the LM134 may have to be reduced, either because of loading problems or because it limits the AC output impedance of the current source. This can be easily accomplished by buffering the LM134 with an FET as shown in the applications. This can reduce capacitance to less than 3 pF and improve

Appendix C – Final Experimental Design

In this section a step by step guide to recreating the final propagation delay experiment will be given.

1) Using a solderless breadboard create the operational amplifier circuit discussed in the *Differential Amplifier Circuit* section. Key Values and Information:
    a. Rf=Rg= 100K Ohms and R1=R2=1K Ohms
    b. LM324 Chipset, Use datasheet to identify pin values
2) Connect the Pressure sensor to the input of the Amplifier circuit using the corresponding datasheets.
3) Using an adjustable air source record the output voltage of the Differential Amplifier Circuit based on the pressure applied to the pressure sensor. This will allow for the calculation of volts per psi. With this number calculate the expected value of volts based on the desired 80 psi. Using the cRIO and Lab View create a program with the same program flow shown by the flow chart below. This process will be repeated 100 times to get more accurate results. Note that Solenoid 2 is connected to the pressure sensor and Solenoid 1 simply releases the system pressure to prevent air accumulation

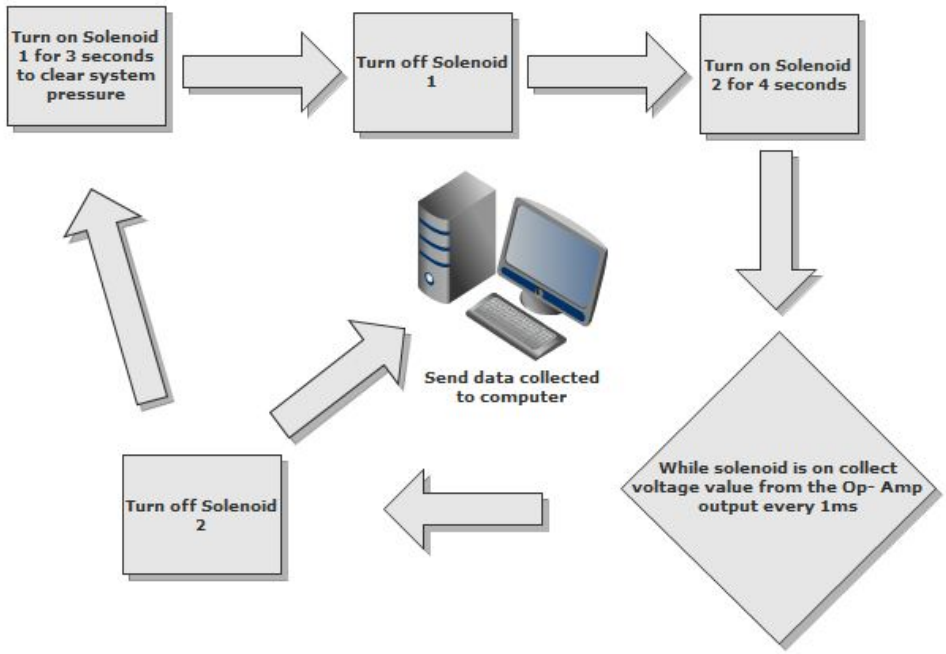

Figure 55 - Flow Chart of cRIO Operation

4) Using the program created in step 4, collect data for the two diameters and the various lengths. These are specified in the sub sections below.
    a. Diameter of 5/32", Lengths of 5',10',15'
    b. Diameter of 1/4", Lengths of 5',10',15'
    c. Solenoid directly connected to pressure sensor
5) Merge the collected data into one excel file for each of the seven tests specified by the different diameters and lengths.
6) Analyze the data using excel to figure out the propagation delay for each of the seven different diameters and lengths

Appendix D – Position Sensor Data Sheet

Model 601-1045

Vishay Spectrol

VISHAY.

Full 360° Smart Position Sensor

FEATURES

- Ratiometric output over 360° range with no dead band
- Self-contained package not requiring external electronic interface
- Angular response 50 µs
- Reverse polarity protection
- Absolute and non volatile positioning output

Pb RoHS COMPLIANT

The model 601-1045 represents a new generation of Smart Sensors. This unique electronic device is a self-contained package which provides an analog electrical output over a full 360° without the need of external electronics. The low power consumption and non-volatile output makes this universal sensor the real cost-effective alternative to encoders. It's versatile design makes it suitable for a variety of industries and applications, such as CCTVs, Medical Instruments, Robotic arm control, CNC machinery, Rotational control systems, Pick n' place machines and Angular feedback applications.

STANDARD ELECTRICAL SPECIFICATIONS	
PARAMETER	
Supply	4.5 to 5.5 V_{DC}
Supply Current	20 mA max.
Absolute Maximum Supply	6 V
Independent Linearity	± 1 % typical
Resolution	Resolves down to a min. of 0.5°
Electrical Track	360° continuous
Analog Voltage Output	Not less than 90 % of supply (ratiometric) - see graphs on next page
Output Ramp Slope	Electrically switchable - see graphs
Output Impedance	1 Ω typical
Temperature Characteristic	± 1° max. over - 40/+ 70 °C
Insulation Resistance	1000 MΩ min.
Dielectric Strength	1000 V_{RMS}, 50/60 Hz

MECHANICAL SPECIFICATIONS	
Rotation	360° continuous
Rotational Speed	5 max. revs/s (duration 60 s)
Operating Torque Maximum	3.68 (0.5) mNm (oz. - in)
Weight	30 g

ENVIRONMENTAL SPECIFICATIONS	
Operating Life	5 000 000 cycles
Operating Temperature Range	- 40 °C to + 70 °C
Storage Temperature Range	- 40 °C to + 105 °C
Sealing	IP54

ORDERING INFORMATION/DESCRIPTION

601-1045	XXXX	B01	e4
MODEL	STANDARD CONFIGURATION CODE	PACKAGING	LEAD FINISH

PRODUCT NUMBER	Ø 1.57 PIN	Ø 3.18 PIN
0000	Yes	Yes
0001	Yes	-
0002	-	Yes
0003	-	-

SAP PART NUMBERING GUIDELINES

601	1045	0001	B01
MODEL	STYLE 1045 or 1056	PIN CONFIGURATION	PACKAGING

Appendix E – Run Speed Test Program

See CD.

Appendix F – Final Experiment Procedure

In this section, a step by step guide to recreating the final speed testing experiment will be given.

1) Create the blast shield to hold the actuator and protect against any unpredictable operation.
2) Couple the encoder to the motor shaft and secure the device within the created blast shield. Make sure the encoder and motor shaft can spin freely without wobble.
3) Connect the encoder to a 5V power source and its output to the analog input port of the cRIO.
4) Using the created VI the program will perform the following operations. First it will run the actuator at the first desired frequency of 500ms for 2 minutes straight recording the encoder position every .25 seconds. The test will perform the 500ms operation for 100 consecutive tests. After completion of these tests the program will then continue the same actions for 250ms, 100ms, 60ms, and 40ms. Data for each test is returned in the form of a Microsoft excel file.
5) The returned data is then merged into a single Microsoft excel file for each frequency run.
6) The data is then analyzed to determine the output speed of the actuator and determine the actuators overall consistency at each frequency.

Appendix G – Torque Testing Setup

1) Secure the motor in the upright position as seen in Figure 56.

Figure 56: Secure Motor

2) Once the actuator is secured attach the torque disk to the drive shaft using the set screw. This is shown in Figure 57.

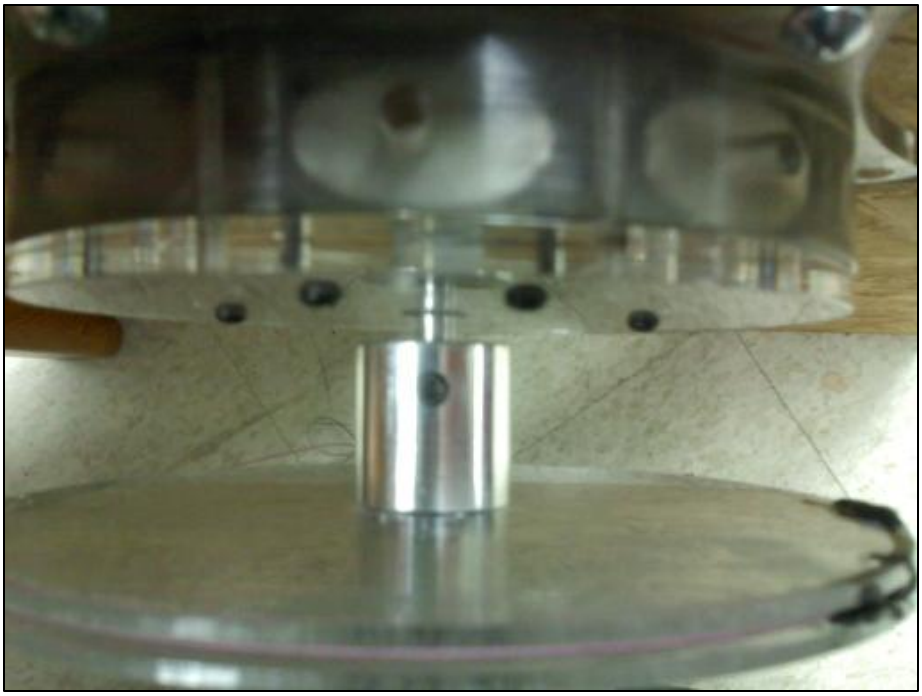

Figure 57: Secured Torque Disk

3) Make sure that all the air connections and solenoid wires are all properly attached. Once this is complete run the program called GUIforrunningmotor.vi.
4) Using the string attached to the torque disk continuously add weights incrementally until the actuator stalls. Once the motor stalls record the last fully operational weight and use it to calculate torque. Torque in this case is equal to the tension in the string multiplied by the radius of the torque disk.

Appendix H – Conversion Factors

From	To	Multiplier	To	Multiplier
N	Kg	0.102	lb	0.22487
Kg	N	9.807	lb	2.2046
Lb	N	4.448	Kg	0.4536

Table 19: Force Units Conversion Factors

From	To	Multiplier	To	Multiplier
Kg/mm	lb/in	55.998	N/mm	9.807
lb/in	Kg/mm	0.017858	N/mm	0.175133
N/mm	Kg/mm	0.101968	lb/in	5.7099

Table 20: Rate Units Conversion Factors

From	To	Multiplier	To	Multiplier	To	Multiplier
in	m	0.0254	ft	0.0833	mm	25.4
mm	m	0.001	ft	0.003281	in	0.0393701

Table 21: Length Units Conversion Factors

Appendix I – Spring Data

Table 22 contains dimensional tolerance data[1,2] for LeeP Plastic Composite Springs (Lee Spring, 2011).

Outside Diameter	
Standard	Metric
.025” to .040” ± .001”	0.64mm to 1.02mm ± .03mm
.057” to .094” ± .003”	1.45mm to 2.36mm ± .08mm
.102” to .250” + .003”–.005”	2.59mm to 6.10mm + .08mm–.13mm
.300” to .500” ± .008”	7.62mm to 12.70mm ± .20mm
.540” to .850” ± .015”	13.97mm to 21.59mm ± .38mm
.875” to 1.125” ± .020”	22.23mm to 28.58mm ± .51mm
1.150” to 1.218” ± .025”	29.21mm to 30.94mm ± .64mm
1.250” to 1.460” ± .030”	31.75mm to 37.08mm ± .76mm
1.480” to 1.687” ± .040”	37.59mm to 42.85mm ± 1.02mm
1.937” to 2.000” ± .055”	49.20mm to 50.80mm ± 1.40mm

Table 22: LeeP Composite Spring Dimensional Tolerances

[1] Spring rate: ± 10%
[2] Solid height: + 5%, no lower limit

Appendix J –Spring Design

Taken from (Lee Spring, 2011).

Compression Springs

To find the load at any working length, when free length and rate are given, use the formula:

$$P = R \times F$$

where:

P is the load in lbs.
R is the rate in lbs. per inch
F is the deflection from free length

Example: (Lee Stock Spring Catalog #LC-032C-8)

Given:

free length of .750”
rate of 22 pounds per inch

Find:

load at 0.5” working length

Solution:

$P = 22 \times .250 = 5.5$lbs.

Extension Springs

To find the load at any working length, when free length and rate are given, use the formula:

$$P = (R \times F) + I.T.$$

where:

P is the load in lbs.
R is the rate in lbs. per inch
F is the deflection from free length
I.T. is the initial tension

Example: (Lee Stock Spring Catalog #LE-031C-1)

Given:

free length of 1.0”
rate of 6.9 pounds per inch
I.T. of 0.7 pounds

Find:

load at 1.5” working length

Solution:

$P = (6.9 \times .500) + 0.7 = 3.45 + .7 = 4.15$ lbs.